Finite element analysis to determine the role of porosity in dynamic localization and fragmentation: Application to porous microstructures obtained from additively manufactured materials

M. Marvi-Mashhadi[a], A. Vaz-Romero[a], F. Sket[b], J. A. Rodríguez-Martínez[a,*]

[a]*Department of Continuum Mechanics and Structural Analysis. University Carlos III of Madrid. Avda. de la Universidad, 30. 28911 Leganés, Madrid, Spain*
[b]*IMDEA Materials Institute, c/Eric Kandel 2, 28906 Getafe, Madrid, Spain*

Abstract

In this paper, we have performed a microstructurally-informed finite element analysis on the effect of porosity on the formation of multiple necks and fragments in ductile thin rings subjected to dynamic expansion. For that purpose, we have characterized by X-ray tomography the porous microstructure of 4 different additively manufactured materials (aluminium alloy $AlSi_{10}Mg$, stainless steel 316L, titanium alloy Ti_6Al_4V and Inconel 718L) with initial void volume fractions ranging from $\approx 0.0007\%$ to $\approx 2\%$, and pore sizes varying between ≈ 6 μm and ≈ 110 μm. Three-dimensional analysis of the tomograms has revealed that the voids generally have nearly spherical shape and quite homogeneous spatial distribution in the bulk of the four materials tested. The pore size distributions quantified from the tomograms have been characterized using a Log-normal statistical function, which has been used in conjunction with a Force Biased Algorithm that replicates the experimentally observed random spatial distribution of the voids, to generate ring expansion finite element models in ABAQUS/Explicit (2016) which include actual porous microstructures representative of the materials tested. We have modeled the materials behavior using von Mises plasticity, and we have carried out finite element calculations for both elastic perfectly-plastic materials, and materials which show strain hardening, strain rate hardening and temperature softening effects. Moreover, we have assumed that fracture occurs when a critical value of effective plastic strain is reached. The finite element calculations have been performed for expansion velocities ranging from 50 m/s to 500 m/s. A key point of this investigation is that we have established individualized correlations between the main features of the porous microstructure (i.e. initial void volume fraction, average void size and maximum void size) and the number of necks and fragments formed in the calculations. In addition, we have brought out the effect of the porous microstrucure and inertia on the distributions of neck and fragment sizes. To the authors' knowledge, this is the first paper ever considering actual porous microstructures to investigate the role of material defects in multiple localization and dynamic fragmentation of ductile metallic materials.

Keywords:

*Corresponding author. Tel. +34 916249904; Fax: +34 916249430. E-mail address: jarmarti@ing.uc3m.es

Additive manufacturing, Printed metals, Porosity, Multiple necking, Fragmentation, Finite elements

1. Introduction

The pioneering statistical theory of Mott (1947) postulated that fragmentation of metals subjected to intense impulsive tensile loads occurs due to the activation of weak points of the material –e.g. material defects like pores, cavities and cracks formed during materials processing– which are scattered throughout the specimen and determine the distribution of fractures sites. It also considered that material failure occurs instantaneously, disregarding the localization of plastic deformation that precedes fracture in ductile metals, as well as the fracture resistance and the fracture energy associated to the breakage process. The instantaneous fracture releases stress waves (or the Mott's waves) that propagate away from the fracture, unloading the specimen. The material cannot continue deforming within the regions of the specimen subjected to the action of the release waves, preventing additional fractures, so that the size of the fragments is determined by the distance traveled by the Mott's waves. Despite the relative simplicity of Mott's theory, and the number of assumptions made to make the model mathematically tractable and applicable to actual engineering problems, Grady (2002) highlighted that Mott's original publication contains seminal theoretical concepts from which numerous later modeling efforts emerged.

For instance, Grady (1981) applied concepts of survival statistics to the theory of Mott to account for spatially random fracture nucleation, and derived fragments size distribution curves that found satisfactory agreement with the experimental data reported by Wesenberg and Sagartz (1977) for thin 6061-T6 aluminum cylinders subjected to rapid radial expansion at strain rates of $\approx 10^4$ s^{-1}. Moreover, Kipp and Grady (1985) expanded the analyses of Mott to explicitly account for energy dissipation during the fracture process, and obtained expressions for the nominal fragment size, the fracture time, and the dynamic fracture strain, which were in reasonable agreement with the experimental data obtained by Grady and Benson (1983) for the fragmentation of OFHC copper and 1100-O aluminum rings subjected to radial expansion at strain rates of $\approx 10^4$ s^{-1}. Grady and Olsen (2003) performed ring expansion fragmentation tests with U6N specimens, for expansion velocities ranging from 50 to 300 m/s, and compared the experimental results with the distribution of fragment masses obtained with Mott's statistical theory and the energy-based fragmentation theory of Kipp and Grady (1985). Both theoretical approaches were in reasonable accord with the experimental data. In addition, the predictions of the energy-based fragmentation theory for the evolution of the number of fragments with the expansion velocity were compared with the experimental evidence, and sensible agreement was found for the whole range of expansion velocities investigated.

Moreover, Zhang and Ravi-Chandar (2006) performed ring expansion experiments using Al 6061-O specimens with rectangular cross-section of thickness 0.5 mm and length 1 mm, at velocities ranging from 80 to 200 m/s, and

measured the distributions of neck spacings and fragment sizes. Following Mott (1947) postulates, Zhang and Ravi-Chandar (2006) suggested that the distribution of lengths between consecutive necks is governed by the spatial distribution of necking strains in the specimen and the unloading waves emanating from growing necks. Relying on Mott (1947) scaling analysis, and assuming that the variation in the necking strain is $\pm 2\%$, Zhang and Ravi-Chandar (2006) determined the necks spacing to be between 17 mm and 7 mm for the lower and higher expansion velocities tested, respectively, being these estimates in good agreement with the experimental results which showed a decrease in the average distance between consecutive necks as the loading rate increases. As to the distribution of fragment sizes, Zhang and Ravi-Chandar (2006) showed that if the length of the fragment is normalized by the characteristic unloading length, the normalized fragment lengths distribution, resulting from putting together the results for different expansion velocities, can be adequately represented by a Weibull probability density function. Zhang and Ravi-Chandar (2006) interpreted this result as an indicator that there is a random distribution of weak points scattered throughout the circumference of the ring, and that the release wave mechanism sets the scale for fragmentation. Zhang and Ravi-Chandar (2008) performed further ring expansion experiments with Al 6061-O, Al 1100-H14 and Cu 101 specimens with different length-to-thickness aspect ratios (different lengths and fixed thickness of 0.5 mm) and different cross-section sizes (varying both length and thickness), for expansion velocities ranging from 65 to 230 m/s. The tests using Al 1100-H14 and Cu 101 specimens with cross section of thickness 0.5 mm and length 1 mm yielded statistical distributions of neck spacings similar to that obtained in the experiments performed with Al 6061-O rings in Zhang and Ravi-Chandar (2006), such that with increasing strain rate, more necks were nucleated at shorter distances. Zhang and Ravi-Chandar (2008) suggested that this behavior occurs at high strain rates because the unloading engendered by any localization does not travel far enough quickly to inhibit further nucleation at neighboring locations. The tests using samples with different cross-section sizes showed that, as the specimen cross-sectional size increases, the strain at the onset of necking, which is roughly the Considère strain for the specimens with the smallest cross-section, increases. The size of the cross-section of the sample also seemed to affect the spatial distribution of necks such that the scatter in the distribution of neck sizes decreases with the increase of the cross-section dimensions. Moreover, the tests using samples with different length-to-thickness ratios showed that the increase of the length of the specimen (thickness was fixed) leads to a decrease of the average neck spacing and to a gradual removal of the long segments without necks that are frequently observed in rings with small length-to-thickness relation. In order to provide further insights into the experimental evidence, Zhang and Ravi-Chandar (2008) performed finite element calculations using ABAQUS/Explicit of specimens with different length-to-thickness ratios expanded at ≈ 250 m/s, modeled with von Mises plasticity and a power-law hardening model, and with material properties corresponding to Al 6061-O. In order to provide an idealized modeling of the material properties variation at the microstructural level, a

random distribution of punctual defects (at the element level), with reduced yield strength and no strain hardening, was included in the samples. As the loading process starts, before the Considère condition was reached, the plastic strain was shown to evolve nearly uniformly over the entire specimen with slight perturbations in the vicinity of the defects. With the continuation of the loading process, there was a magnification of the strain fluctuations, so that for the specimens with the smallest cross-section multiple localized necks formed right after the Considère strain was met. In contrast, for specimens with large length-to-thickness ratio, the calculations revealed the emergence of a *large* post-uniform deformation regime, so that the localization, that took the form of multiple necking bands, developed when the average strain in the specimen was more than twice the Considère strain (which corresponds to the bifurcation strain for the sheet necking mode given by Hill (1952)).

The influence of defects on necking localization and the formation of multiple necks for strains well beyond the Considère condition was also the subject of study of Vaz-Romero et al. (2017), who performed finite element calculations of nonlinear elastic bars with spatially-localized defects of the strain rate field and subjected to dynamic stretching. The computations of Vaz-Romero et al. (2017) showed that the post-uniform deformation regime that extends from the Considère strain until the formation of localized necks enlarges with the strain rate, bringing out the stabilizing effect of inertia which delays localization. The finite element results of Vaz-Romero et al. (2017) also showed that, while the defects of the strain rate field speed up the development of the necking pattern in the late stages of the localization process, the characteristic (average) distance between consecutive necks is largely independent of the defects for the defects' amplitudes investigated. The average neck spacing obtained with the finite elements was compared with the predictions of 1D and 3D dynamic stability analyses, finding good correlation for strain rates varying between 200 s^{-1} and 10000 s^{-1}. The agreement between numerical calculations and linear stability analyses was considered to be a proof that the multiple localization mechanisms cannot be effectively explained using exclusively statistical theories. Similarly, it was also suggested that the distance between necks cannot be exclusively attributed to the random distribution of material properties and to the defects population (see Dequiedt (2015)). Following previous works of Fressengeas and Molinari (1994), Guduru and Freund (2002) and Mercier et al. (2010) among others, Vaz-Romero et al. (2017) indicated that there are dominant necking modes which define, at least up to some extent, the average neck spacing in multiple localization patterns, the specific dominant modes being determined by the emergence of inertia effects at high strain rates. The effect of material defects on the formation of multiple necking patterns was also investigated by N'souglo et al. (2018), who performed finite element calculations of elasto-plastic bars with yielding modeled with Gurson porous plasticity criterion (Gurson, 1977; Tvergaard, 1981, 1982) and subjected to dynamic tension at strain rates varying from 10^3 s^{-1} to $5 \cdot 10^4$ s^{-1}. The initial porosity, which in the Gurson model (Gurson, 1977; Tvergaard, 1981, 1982) intends to idealize material defects, was randomly varied at the element level, using various

upper and lower bounds for the maximum and minimum porosity variation, and different spatial distributions. The calculations of N'souglo et al. (2018) indicated that, for the lower strain rates, the distribution of neck spacings is heterogeneous and sensitive to the initial distribution of the porosity. In contrast, as the strain rate increases, the distribution of lengths between consecutive necks becomes more homogeneous and less dependent on the initial distribution of porosity. A possible explanation for these results was sought on the predictions of a linear stability analysis, which brought out that with the increase of the strain rate the dominant necking modes have a strong prevalence over the other growing modes, reducing the scatter in the distribution of neck sizes. Other authors who performed numerical calculations to investigate the influence of material defects on multiple localization and fragmentation problems are Hiroe et al. (2008), Zhang and Ravi-Chandar (2010), Liu et al. (2013, 2016) and Cliche and Ravi-Chandar (2018). In these works, as in those mentioned above, material defects are included by allocating a reduced elastic limit to an arbitrary number of material points, or by assuming local variations in the failure strain. However, while this strategy to model material defects is easy to implement in numerical calculations, and thus it shows clear advantages from a practical standpoint, it is a difficult task to associate these idealized defects with actual microstructural heterogeneity or mechanical property variations, and hence to elucidate what is the role of actual material flaws in the formation of multiple localization patterns and the dynamic fragmentation of metallic structures. Furthermore, most of the times the actual distribution of defects in the material is not known.

These are precisely the gaps we intend to fill in this paper. For that purpose, we have devised a microstructurally-informed finite element analysis to determine the role of actual porosity, i.e. actual material defects, on the formation of multiple necks and fractures in metallic rings subjected to radial expansion. We have characterized by X-ray tomography the porous microstructure of 4 different additively manufactured materials (aluminium alloy $AlSi_{10}Mg$, stainless steel 316L, titanium alloy Ti_6Al_4V and Inconel 718L) with initial void volume fractions ranging from $\approx 0.0007\%$ to $\approx 2\%$, and roughly spherical pores with diameter varying between ≈ 6 μm and ≈ 110 μm. The pores recorded in the X-ray tomograms are fitted to a Log-normal statistical function that is later used to generate porosity distributions based on the actual microstructure of the material. These porosity distributions are then included in the finite element model of a ring subjected to rapid radial expansion so that the specimen contains actual voids. We have performed calculations for expansion velocities ranging from 50 m/s to 500 m/s, assuming that the matrix material follows von Mises plasticity. Specifically, we assume that the matrix material is elastic perfectly-plastic in Section 4, and thermo-viscoplastic with strain hardening, strain rate hardening and thermal softening in Section 5. For simplicity, material fracture is assumed to occur when a critical effective plastic strain is reached. Note that the objective of this paper is to determine the effect of porous microstructure on dynamic localization and fragmentation, and we do not pay attention to the specific mechanical response of the printed metals from which the microstructures are taken. The results of the finite element simulations provide new insights

into the role of porosity on the distributions of necks spacing and fragments size. While direct numerical simulation of specimens containing a large population of voids was performed by Becker and Callaghan (2018, 2020) to assess the load path and mean stress dependence of void growth, to the authors' knowledge, this is the first paper ever that includes actual microstructural porosity distributions in large scale calculations of dynamic localization and multiple ductile fracture.

2. Porosity distribution

In this section, we describe the methodology that we have developed to determine the distribution, shape and size of the pores present in several additively manufactured metals. Recall that in this paper we do not study the mechanical behavior of the materials investigated, the additively manufactured materials are solely employed to obtain representative porosity distributions to be used in the simulations of Sections 4 and 5. Cylindrical specimens with diameter and height of 6 mm were printed by Selective Laser Melting (SLM) by the company Materialise out of aluminium alloy $AlSi_{10}Mg$, stainless steel 316L, titanium alloy Ti_6Al_4V and Inconel 718L. This printing technique often leads to residual porosity in the samples, generally lower than 5%, which can be controlled adjusting the major printing parameters (Aboulkhair et al., 2014; Kasperovich et al., 2016; Moussaoui et al., 2018). Two different printing directions of parallel and perpendicular to the longitudinal axis of the cylinder were chosen. We have analyzed 12 specimens (i.e. 12 porous microstructures) which are denoted as Al3Z, Al3XY, Al0.5Z, Al0.5XY, SS5Z, SS5XY, SS0.5Z, SS0.5XY, Ti0.5Z, Ti0.5XY, INC1Z and INC1XY, where Al, SS, Ti and INC stand for the material, the following numbers indicate the nominal void volume fraction (%) provided by the manufacturer, and Z and XY determine whether the sample was printed in parallel or perpendicular direction to the longitudinal axis of the cylinder. We performed X-ray Computed Tomography (XCT) of each sample using a Nanotom 160NF tomograph (General Electric-Phoenix) located at IMDEA Materials Institute. We used a $3 \times 3 \times 3$ μm^3 tomogram voxel size. The reconstruction of the tomograms was carried out using an algorithm based on the filtered back-projection procedure for Feldkamp cone beam geometry (e.g. see Stef et al. (2018)). Further analysis of 3D reconstructed images was performed using the open source software tool ImageJ (Schneider et al., 2012), so that for each sample we selected three cylindrical sub-volumes of 1.5 mm diameter and 1.5 mm height, with no overlapping between them, to obtain the distribution, shape and size of the voids in the specimens investigated. Analyzing three cylindrical sub-volumes for each sample, with the aforementioned dimensions, enables to record sufficient number of voids to obtain statistically significant results which are representative of the actual porosity distribution in the materials (note that the 3D object counter plugin of ImageJ (Bolte and Cordeliéres, 2006) does not allow to analyze the $AlSi_{10}Mg$ cylindrical samples of 6 mm height and 6 mm diameter in one step due to the very large number of voids they contain).

Figs. 1-4 show 2D XCT images of the middle cross-section of the samples perpendicular to the main axis of the cylinder for the 12 specimens investigated. The voids appeared in form of dark spots, with roughly circular area, which are randomly dispersed in the samples. Notice that there is a layer of larger voids close to the outer shell of the cylinders. Sukal et al. (2018) and Koutiri et al. (2018), among others, stated that the concentration of pores below the surface of SLM printed parts is caused by the inadequate connection of the hatching of the sample volume with the contour of the part. This layer of larger voids is excluded from the calculations used to characterize the porosity distribution of the materials in order to maintain a homogeneous microstructure. Notice that the number of voids in the $AlSi_{10}Mg$ samples is greater than in the other materials tested (as mentioned before), with important differences between the samples with nominal porosity 3% and 0.5%, so that the specimens Al3XY and Al3Z contain more voids which are generally slightly larger (see also Table 1). Moreover, stainless steel 316L and titanium alloy Ti_6Al_4V specimens have the lower levels of porosity. A more detailed quantitative analysis of the void volume fraction of the specimens and the distribution of void sizes is carried out below.

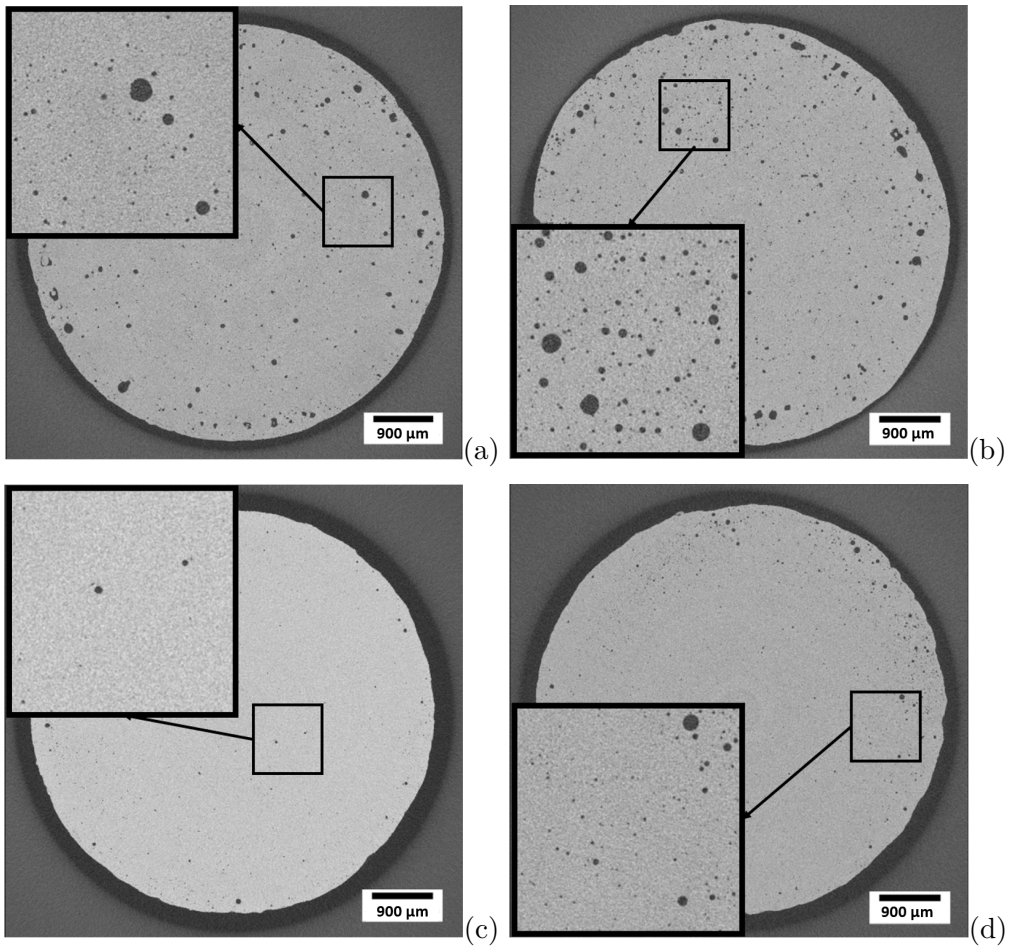

Figure 1: X-ray computed tomography images of the middle cross-section of the samples perpendicular to the main axis of the cylinder for: (a) Al3Z, (b) Al3XY, (c) Al0.5Z and (d) Al0.5XY. The dark spots correspond to porosity. The pixel size is 3 μm.

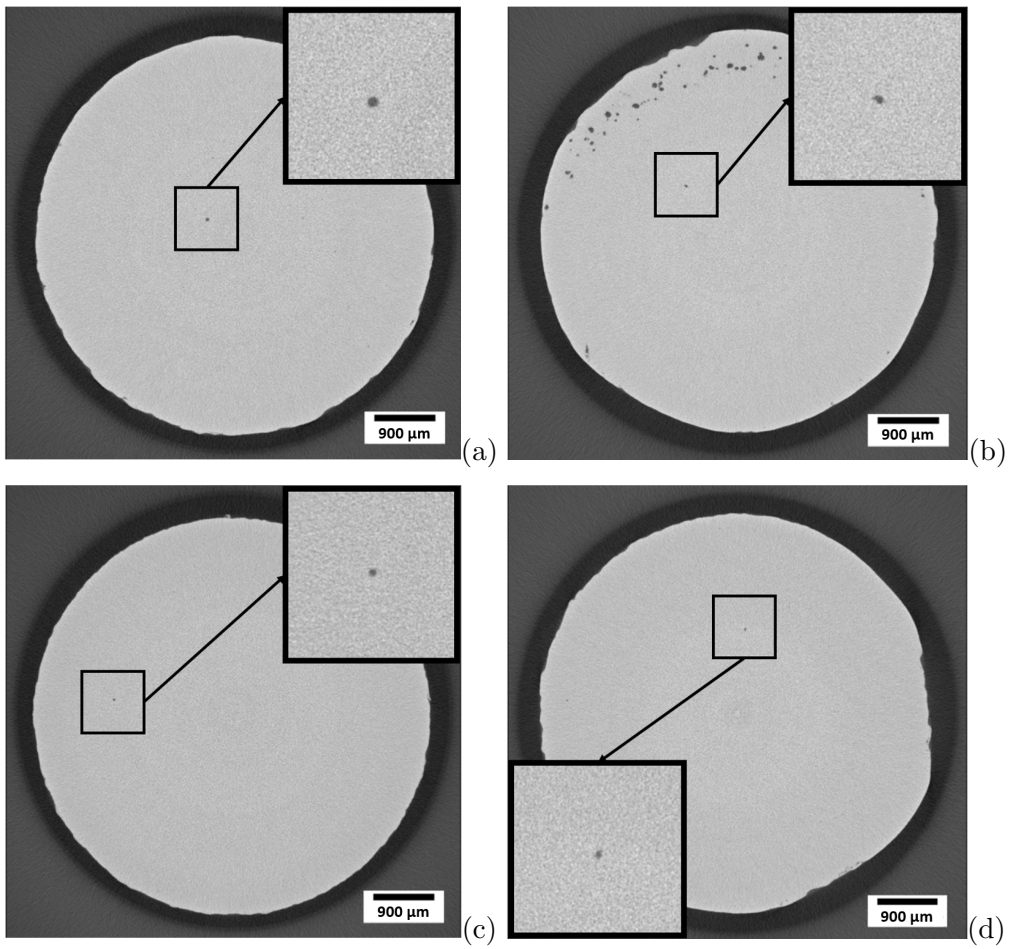

Figure 2: X-ray computed tomography images of the middle cross-section of the samples perpendicular to the main axis of the cylinder for: (a) SS5Z, (b) SS5XY, (c) SS0.5Z and (d) SS0.5XY. The dark spots correspond to porosity. The pixel size is 3 μm.

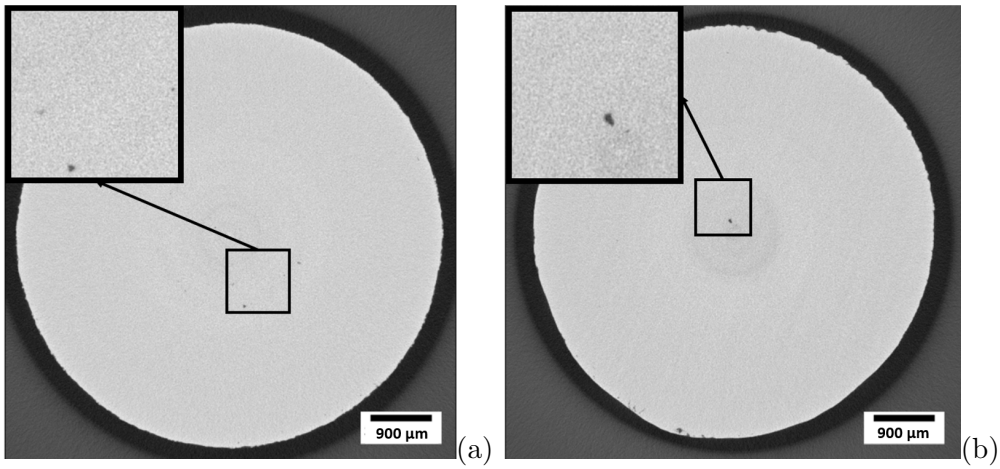

Figure 3: X-ray computed tomography images of the middle cross-section of the samples perpendicular to the main axis of the cylinder for: (a) Ti0.5Z and (b) Ti0.5XY. The dark spots correspond to porosity. The pixel size is 3 μm.

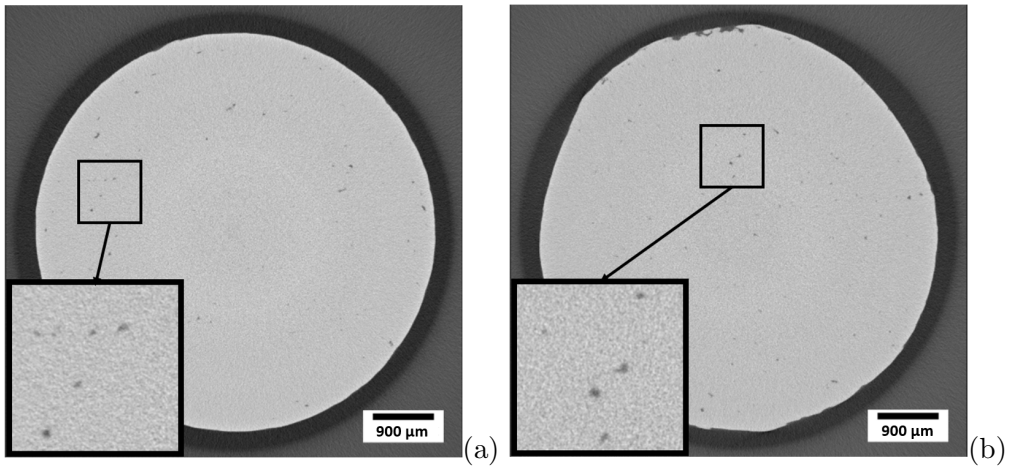

(a) (b)

Figure 4: X-ray computed tomography images of the middle cross-section of the samples perpendicular to the main axis of the cylinder for: (a) INC1Z and (b) INC1XY. The dark spots correspond to porosity. The pixel size is 3 μm.

Figs. 5-8 show 3D rendered images of the porosity distribution (in orange) in the cylindrical sub-volumes. Note that we only show 1 out of the 3 cylindrical sub-volumes with diameter and height of 1.5 mm that we have analyzed per sample. Consistent with the 2D XCT images shown in Figs. 1-4, the 3D reconstructions make apparent that the $AlSi_{10}Mg$ samples have the largest number of voids, being Inconel 718L the material with the next largest number of pores, followed by stainless steel 316L and titanium alloy Ti_6Al_4V, for which the void volume fraction is the lowest. For all the specimens, the voids, which are *roughly* spherical (see Zhang et al. (2017)), are *rather* homogeneously/uniformly distributed in the bulk of the material (note that the Inconel 718L specimens also show flattened pores, most likely due to lack of fusion, nevertheless, we assume that all voids can be considered spherical for the modeling purposes, see Section 3). A summary of the measurements obtained from the reconstructed 3D tomograms is stressed in Table 1. The void volume fraction and the number of voids per mm^3 are computed by averaging the results obtained with the three cylindrical sub-volumes that we have analyzed per sample to characterize materials porosity (the total material volume analyzed per sample is ≈ 8 mm^3). Note that the measured void volume fractions are lower than the nominal values indicated by the supplier. This occurs, most likely, because the large voids near the outer shell of the cylinders and the voids with diameter less than 6 μm were excluded from the calculations (voids with diameter smaller than 6 μm cannot be detected with the resolution of $3 \times 3 \times 3$ μm^3 of voxel size).

The XCT measurements of void size distributions are represented in Figs. 9-12 in form of relative frequency versus void diameter (black columns). The void distributions have been computed using all pores recorded in the three cylindrical sub-volumes that we have analyzed per sample. Note that we have considered a continuous probability density function, so that the histogram bins are just selected to illustrate the evolution of the number of voids with the voids size. The experimental measurements have been fitted to the Log-normal distribution (solid

red line) with corresponding mean (μ) and standard deviation (dev) values given in Table 1. The number of voids with diameter larger than 75 μm is very small in comparison with the total number of voids, so that 75 μm is the largest pore size considered in Figs. 9-12. The limitation of the void diameter to 75 μm in the graphs is for illustrative purposes only, to not increase the scale of the plots. However, in the finite element models we include pores with diameter greater than 75 μm (see Section 3), as recorded from the tomograms. Notice that the only microstructures containing pores with diameter greater than 75 μm are Al3Z, Al3XY, SS5Z and INC1Z, see Table 1. For all materials and specimens investigated, the diameter of most voids lies within the range 5 μm $< d <$ 30 μm. The greatest and the smallest average pore sizes, 18.45 μm and 6.41 μm, correspond to the specimens SS5Z and INC1XY, respectively. Moreover, the standard deviation of the distributions lies between 3.81 μm for Al0.5Z and 9.85 μm for SS5Z. Notice that there is no clear effect of the printing orientation on the average pore size. While for $AlSi_{10}Mg$ and Ti_6Al_4V the average diameter of the voids is smaller when the printing direction is parallel to the longitudinal axis of the cylinder, the opposite trend is obtained for stainless steel 316L and Inconel 718L. Similarly, there is no correlation between the printing direction and the standard deviation of the distributions of pores sizes, neither between the printing direction and the maximum size of the voids.

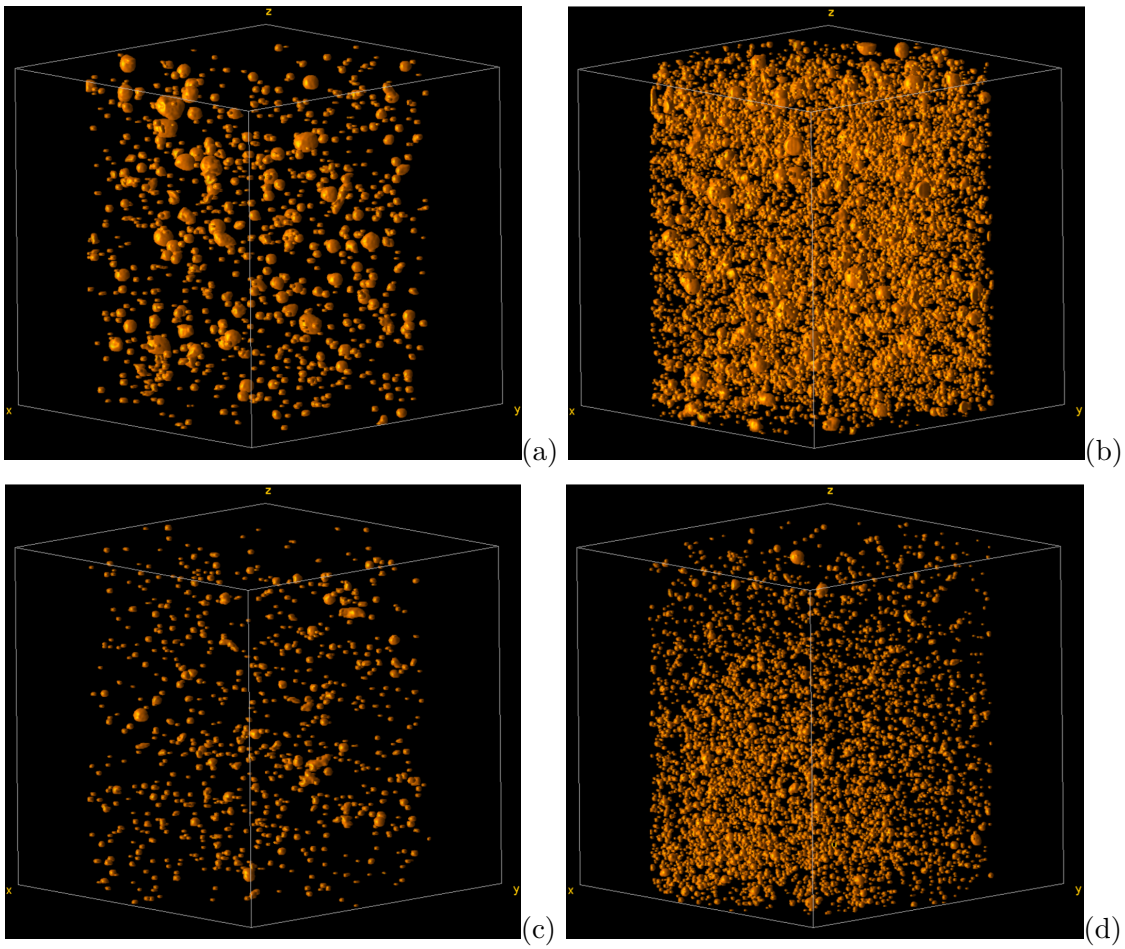

Figure 5: 3D reconstruction of cylindrical sub-volume with diameter 1.5 mm and height 1.5 mm for: (a) Al3Z, (b) Al3XY, (c) Al0.5Z and (d) Al0.5XY. Porosity distribution in orange. For interpretation of the references to colour in the text, the reader is referred to the web version of this article.

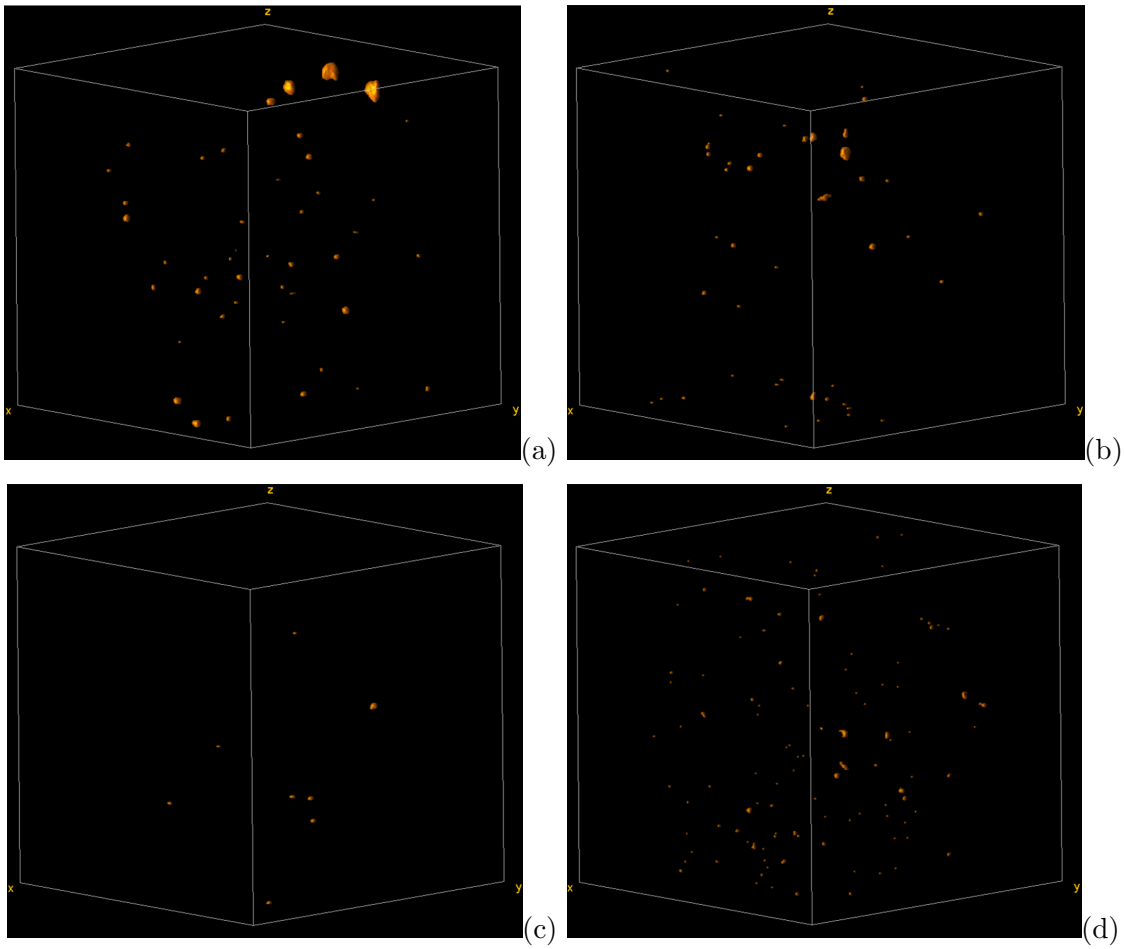

Figure 6: 3D reconstruction of cylindrical sub-volume with diameter 1.5 mm and height 1.5 mm for: (a) SS5Z, (b) SS5XY, (c) SS0.5Z and (d) SS0.5XY. Porosity distribution in orange. For interpretation of the references to colour in the text, the reader is referred to the web version of this article.

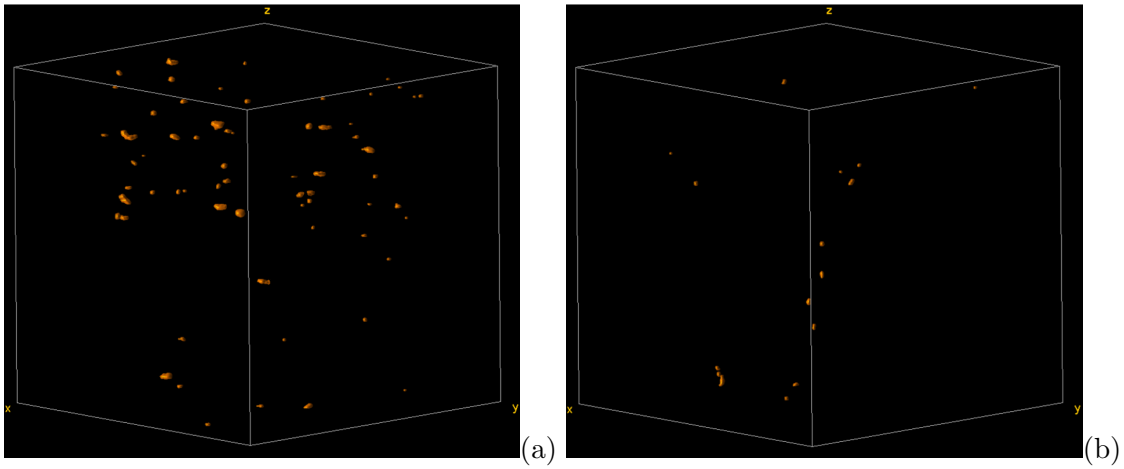

Figure 7: 3D reconstruction of cylindrical sub-volume with diameter 1.5 mm and height 1.5 mm for: (a) Ti0.5Z and (b) Ti0.5XY. Porosity distribution in orange. For interpretation of the references to colour in the text, the reader is referred to the web version of this article.

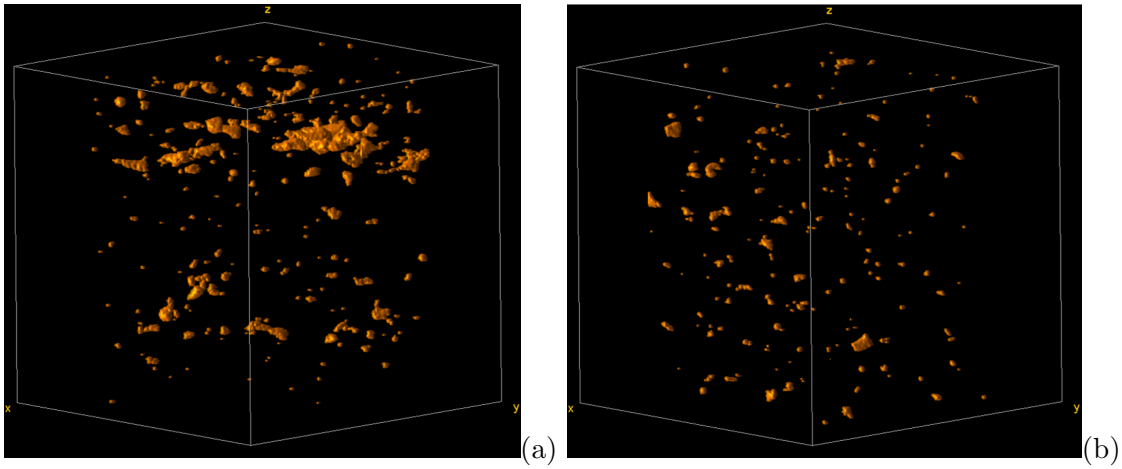

Figure 8: 3D reconstruction of cylindrical sub-volume with diameter 1.5 mm and height 1.5 mm for: (a) INC1Z and (b) INC1XY. Porosity distribution in orange. For interpretation of the references to colour in the text, the reader is referred to the web version of this article.

	Al3Z	Al3XY	Al0.5Z	Al0.5XY	SS5Z	SS5XY	SS0.5Z	SS0.5XY	Ti0.5Z	Ti0.5XY	INC1Z	INC1XY
VF (%)	1.15	2.17	0.13	0.14	0.0290	0.0025	0.0007	0.0026	0.0033	0.0013	0.1363	0.0203
Voids (num./mm^3)	2500	5985	962	810	18	17	4	38	18	5	147	390
d_{max} (μm)	107.00	110.53	58.50	41.24	100.00	41.40	25.90	29.40	31.44	26.93	78.93	45.52
d_{min} (μm)	8.02	8.00	8.1	8.01	7.44	7.40	8.06	8.01	7.44	8.27	7.45	6.36
μ (μm)	11.31	15.98	10.50	15.54	18.45	11.21	11.23	6.83	14.30	17.30	16.58	6.41
dev (μm)	5.03	4.57	3.81	4.37	9.85	5.13	5.04	6.70	9.31	5.03	7.71	4.56

Table 1: Summary of the measurements obtained from the reconstructed 3D tomograms: initial void volume fraction (VF), number of voids per mm^3 (Voids), maximum diameter of voids (d_{max}), minimum diameter of voids (d_{min}), and mean (μ) and standard deviation (dev) values of fitted Log-normal distribution.

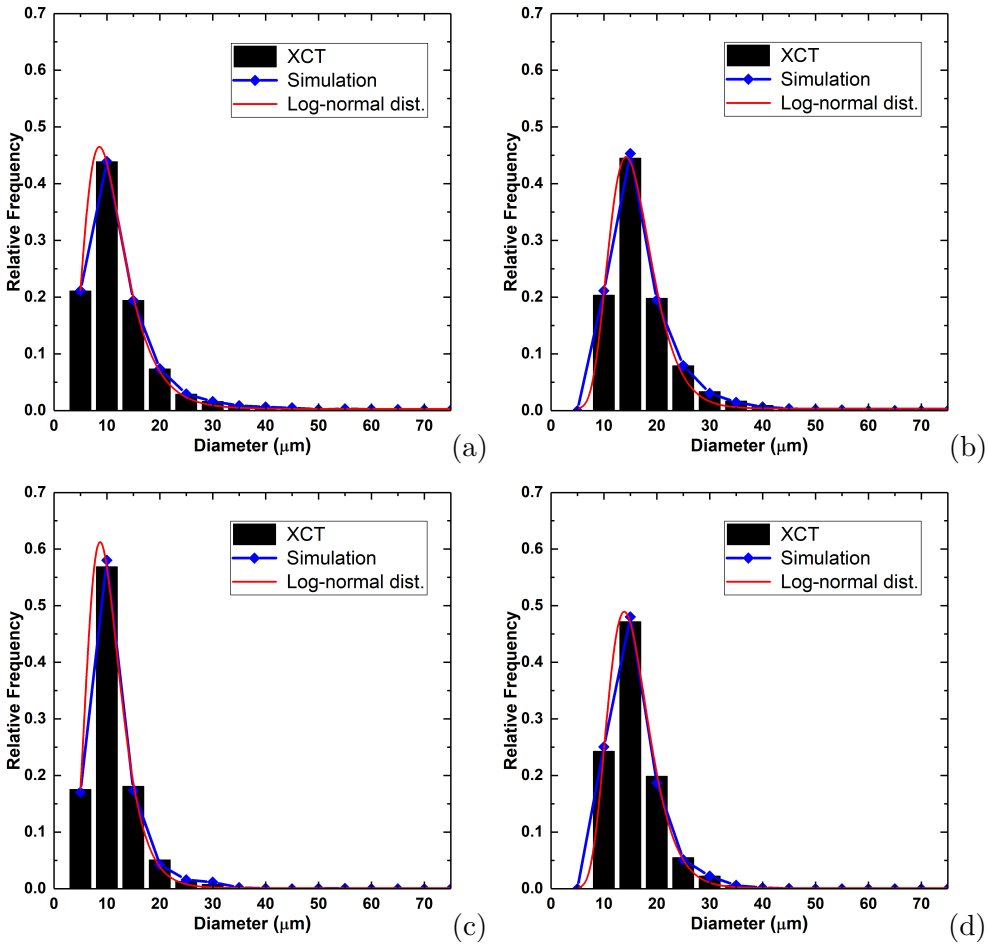

Figure 9: Void size distribution corresponding to: (a) Al3Z, (b) Al3XY, (c) Al0.5Z and (d) Al0.5XY. The Log-normal distribution function was fitted (solid red line) to the X-ray computed tomography measurements (black columns). The blue line represents the void size distribution included in the ring expansion model developed in ABAQUS/Explicit (2016) for one of the three realizations used in the finite element calculations (R1, R2, R3), see Section 3. For interpretation of the references to colour in the text, the reader is referred to the web version of this article.

3. Finite element modeling

In this section, we present the ring expansion finite element model that we have created to study the role of porous microstructure in dynamic localization and fragmentation of ductile materials. Following the works of Rusinek and Zaera (2007), Vadillo et al. (2012) and Rodríguez-Martínez et al. (2013b), we have modeled in ABAQUS/Explicit (2016) a thin ring with inner and outer radii $R_{in} = 15$ mm and $R_{out} = 15.5$ mm, respectively, and axial thickness $e = 0.5$ mm, subjected to rapid radial expansion, see Fig. 13. The radial thickness will be referred to as $h = R_{out} - R_{in}$. Similar specimen dimensions were used in the ring expansion experiments performed by Zhang and Ravi-Chandar (2006). The loading condition is a radial velocity, V_r, applied in the inner surface of the ring which remains constant throughout the entire analysis (Rusinek and Zaera, 2007; Vadillo et al.,

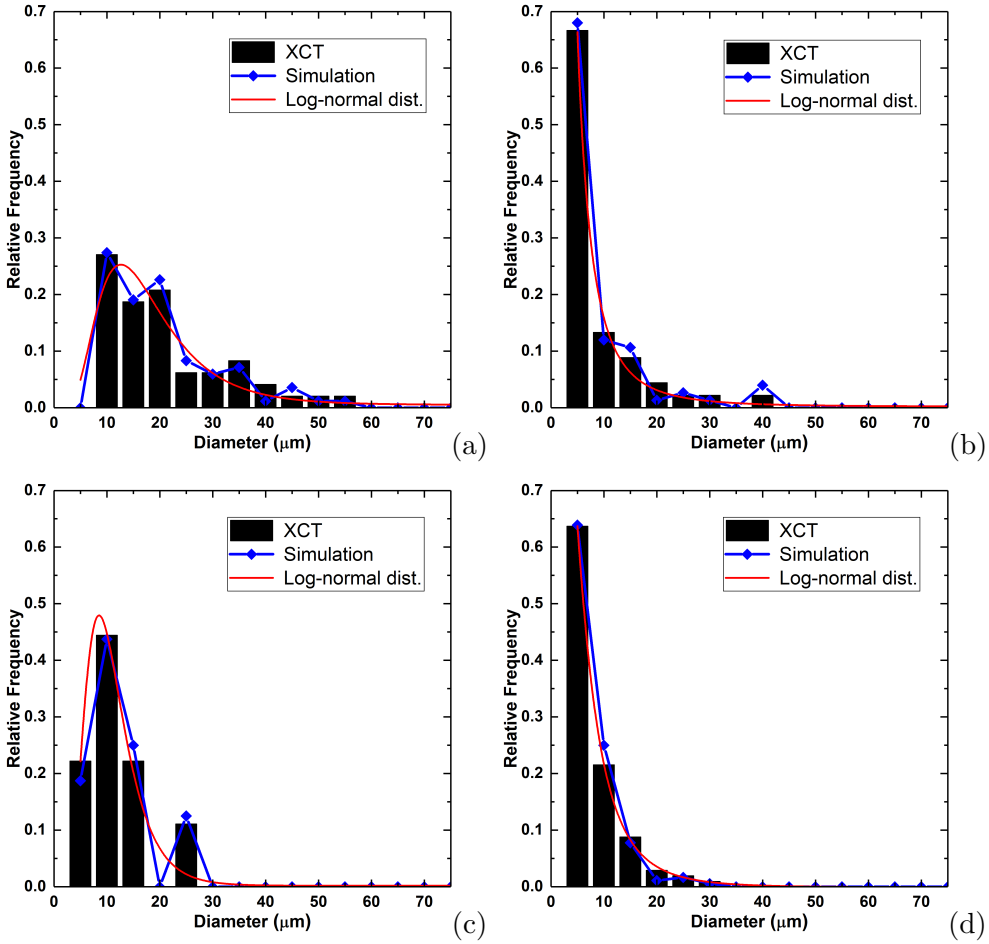

Figure 10: Void size distribution corresponding to: (a) SS5Z, (b) SS5XY, (c) SS0.5Z and (d) SS0.5XY. The Log-normal distribution function was fitted (solid red line) to the X-ray computed tomography measurements (black columns). The blue line represents the void size distribution included in the ring expansion model developed in ABAQUS/Explicit (2016) for one of the three realizations used in the finite element calculations (R1, R2, R3), see Section 3. For interpretation of the references to colour in the text, the reader is referred to the web version of this article.

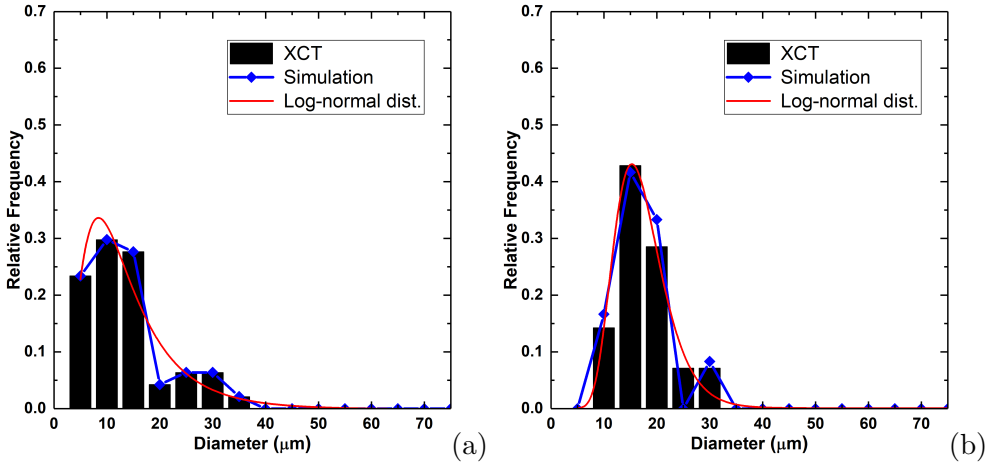

Figure 11: Void size distribution corresponding to: (a) Ti0.5Z and (b) Ti0.5XY. The Log-normal distribution function was fitted (solid red line) to the X-ray computed tomography measurements (black columns). The blue line represents the void size distribution included in the ring expansion model developed in ABAQUS/Explicit (2016) for one of the three realizations used in the finite element calculations (R1, R2, R3), see Section 3. For interpretation of the references to colour in the text, the reader is referred to the web version of this article.

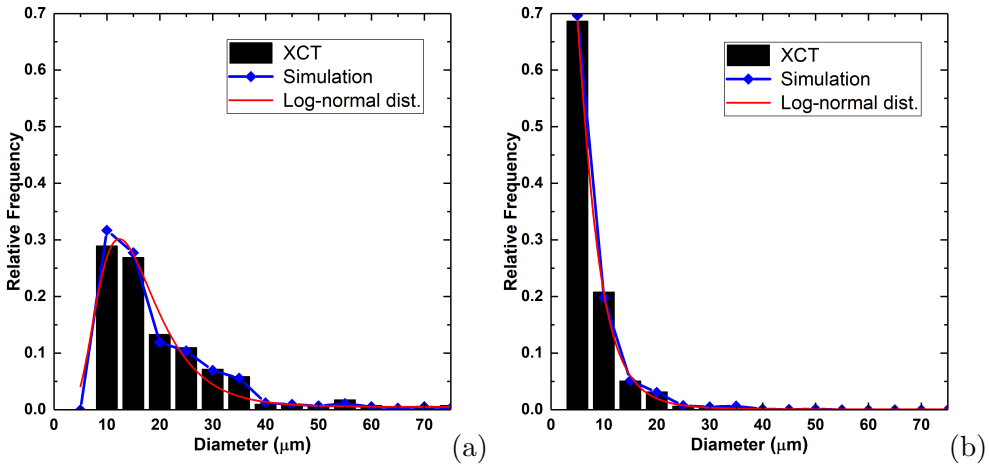

Figure 12: Void size distribution corresponding to: (a) INC1Z and (b) INC1XY. The Log-normal distribution function was fitted (solid red line) to the X-ray computed tomography measurements (black columns). The blue line represents the void size distribution included in the ring expansion model developed in ABAQUS/Explicit (2016) for one of the three realizations used in the finite element calculations (R1, R2, R3), see Section 3. For interpretation of the references to color in the text, the reader is referred to the web version of this article.

2012; Rodríguez-Martínez et al., 2013b; Vaz-Romero et al., 2019). The initial condition is a radial velocity of the same value $V(t=0) = V_r$ applied to all the nodes of the finite element mesh (Vaz-Romero et al., 2019; Marvi-Mashhadi and Rodríguez-Martínez, 2020). The application of this initial condition minimizes the propagation of waves through the thickness of the ring due to the abrupt motion of the inner surface at $t = 0$. Otherwise, the waves generated due to the application of the loading condition could lead to instantaneous plastic localization in the inner surface of the specimen (Needleman, 1991; Xue et al., 2008; Vaz-Romero et al., 2019). We are aware that these initial and loading conditions idealize the velocity boundary conditions generally observed in laboratory experiments. However, imposing a constant radial velocity shows the advantage that the nominal strain rate along the loading process is constant, which facilitates the comparison with analytical models and other finite element calculations reported in the literature which use similar loading condition, see Figs. 22 and 31. The initial strain rate in the material is $\dot{\varepsilon}_0 \approx \frac{V_r}{R_{in}}$. We have performed calculations with different loading velocities ranging from 50 m/s to 500 m/s, i.e. the initial strain rate varies between ≈ 3333 s^{-1} and ≈ 33333 s^{-1}. While the largest expansion velocities considered exceed the regular experimental capabilities (ring expansion tests can rarely be performed for velocities higher than 300 m/s, see Grady and Benson (1983), Grady and Olsen (2003) and Zhang and Ravi-Chandar (2006)), exploring such a wide range of loading rates helps to enlighten the role of porous microstructure on the formation of multiple necks and fragments. Note that we have only analyzed a quarter of the ring (for the microstructure Al3XY only an eighth) in order to reduce the computational time, since we need to use very fine mesh to define the actual distribution of porosity in the microstructures investigated (see the discussion below).

The novelty of the finite element analysis performed in this paper is that we have included in the ring the actual pores recorded in the tomograms. To this end, the voids are modeled as spheres characterized by the coordinates of their centers, which are referred to a Cartesian coordinate system with origin located at the center of mass of the whole specimen (X, Y, Z) (see Fig. 13), and the corresponding diameters d_i, where the sub-index i denotes the sphere number. Recall that most of the voids recorded in the XCT images presented in Figs. 5-8 showed nearly spherical shape, and we did not notice any specific effect of the printing orientation on the shape of the voids, so that taking the voids to be spherical seems to be a reasonable assumption, which in turn facilitates the generation of the finite element models and the interpretation of results. Nevertheless, the methodology presented in this paper can be easily adapted to consider, for instance, oblate and prolate spheroidal voids with different orientations (this is left for a future work). Moreover, the number of pores and the distribution of pore sizes included in the ring are determined using a Log-normal distribution with parameters obtained from the tomograms and specified in Table 1. Recall that with the resolution of $3 \times 3 \times 3$ μm^3 of voxel size used in the X-ray tomography we did not detect pores with diameter smaller than 6 μm, so that this is the smallest pore size included in the finite element models. Furthermore, we have randomly distributed the pores in the ring, which is consistent with the fact that the voids are *rather* uniformly/homogeneously dispersed in most of the samples investigated, see Figs. 5-8. Random positions of the sphere centers are obtained by means of a Force Biased Algorithm (Bargieł and Mościński, 1991). Nevertheless, note that the random distribution of voids allows for having pore clusters, leading to specific portions of the ring with large void volume fraction (see Fig. 16). Note also that, while the maximum void volume fraction of the printed samples studied in this paper is 2.13% (see Table 1), this algorithm, which is frequently used to design highly porous media such as foams (Marvi-Mashhadi et al., 2020), is able to generate random packed configurations of spheres with a predefined size distribution and volume fraction up to 60%, and thus the methodology developed in this paper can be applied to model the porous microstructure of printed or sintered metals with larger porosity.

The specific steps taken to generate the porous microstructure are as follows. Firstly, the Force Biased Algorithm generates an initial spatial distribution of M spheres $S(X_i, Y_i, Z_i, d_i)$, where X_i, Y_i and Z_i are the coordinates of the centers of the spheres and d_i is taken from the XCT measurements, in a cubic volume element of $1 \times 1 \times 1$ mm^3, using the Log-normal function parameters given in Table 1 to determine the distribution of void sizes. The dimensions of the cubic volume element enable to include sufficient number of voids to obtain statistically significant results which are representative of the actual porosity distribution in the materials. Initially, overlapping of spheres is allowed. Then, the algorithm starts to reduce the overlaps between spheres by pushing apart spheres that are connected. After specific number of iterations, relocation of overlapped spheres is stopped and the remained

overlapped spheres are gradually shrunk to remove all connections, while the non-overlapped spheres are enlarged accordingly to fulfill the Log-normal distribution of void sizes. The final outcome of the algorithm is a new packed non-overlapped configuration of spheres $S^{'}(X_i', Y_i', Z_i', d_i')$ with number of voids and distribution of void sizes consistent with the XCT measurements. Note that X_i', Y_i' and Z_i' are the new coordinates of the centers of the spheres, and d_i' is the new diameter of i^{th} sphere. This operation is repeated to obtain $N = 24$ random packed configurations of $1 \times 1 \times 1$ mm^3 in order to generate the porous microstructure of the finite element model (a quarter of the circumference of the ring is approximately 24 mm). Note that there are no spheres intersecting the boundaries of the 24 packed configurations used to build the ring. Moreover, denoting $X'_{m,j}$ as the X coordinate of the m^{th} sphere ($m = 1, \ldots, M$) belonging to the pack configuration j ($j = 1, \ldots, N$), then, to align all the packed configurations on the X-axis:

$$X_i'' = (j-1) + X'_{m,j}, \text{ with } i = 1, ..., N \times M \text{ and } j = 1, ..., N \text{ and } m = 1, ..., M \tag{1}$$

where X_i'' is the new X coordinate of the i^{th} sphere. Note that $Y_i'' = Y_i'$ and $Z_i'' = Z_i'$. Moreover, equation (2) places the packed configurations on the inner circumference of the ring:

$$\begin{aligned} X_i''' &= \left(Y_i'' + R_{in}\right) \cos\left(\frac{X_i''}{R_{in}}\right) \\ Y_i''' &= \left(Y_i'' + R_{in}\right) \sin\left(\frac{X_i''}{R_{in}}\right) \\ Z_i''' &= Z_i'' \end{aligned} \tag{2}$$

where X_i''', Y_i''' and Z_i''' are the new coordinates for the i^{th} sphere. Notice that the cross-section of the specimen created in ABAQUS is 0.5×0.5 mm^2, i.e. it is smaller than the cubic volume element of $1 \times 1 \times 1$ mm^3 used to pack the spheres, and therefore approximately three quarters of the spheres lie outside the ring boundaries (recall that the dimensions of the cubic volume element were taken greater than the cross-section of the ring in order to include sufficient number of voids to obtain statistically significant results which are representative of the actual porosity distribution in the materials). Thus, the out-of-ring-boundary spheres as well as the spheres overlapping with the outer walls of the ring were dismissed, see Fig. 13(a). Next, the spheres which lie inside the specimen boundaries were cut out to obtain actual voids inside the ring model. For each of the 12 samples analyzed (see Section 2) we have generated three realizations of void size and position distribution fulfilling the same Log-normal function in order to take into account the potential scatter in the finite element results coming from the randomness in void dispersion. These three realizations will be denoted as R1, R2 and R3, respectively. It is worth mentioning that the whole process to create the porous microstruture was automatized using a Python script which generates the command file for ABAQUS/CAE to create the porous ring.

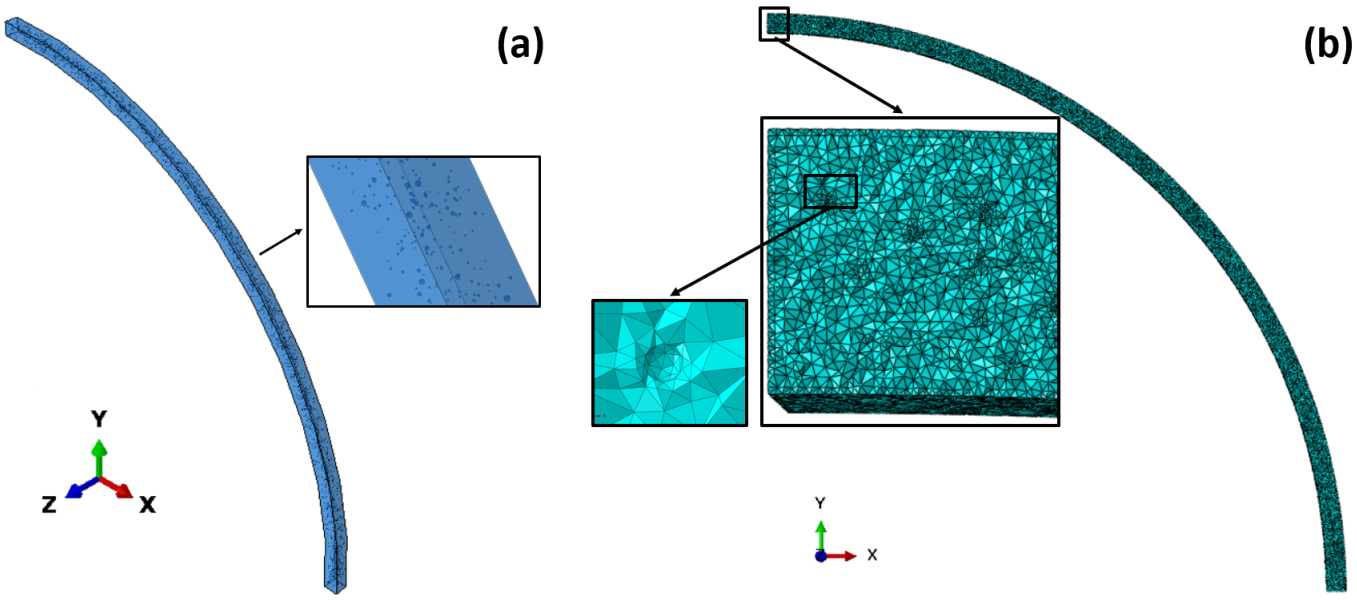

Figure 13: Finite element model created in ABAQUS/Explicit (2016) for realization R1 of the microstructure INC1XY. The Cartesian coordinate system (X, Y, Z) has the origin located at the center of mass of the whole specimen. (a) Virtual design of the porous ring. (b) Discretized model. The zoomed frame shows the mesh quality and accuracy of the voids description.

The agreement between the virtual porous microstructure of the rings modeled in ABAQUS/Explicit (2016) and the actual porous microstructure of the specimens studied is apparent in Figs. 9-12, where the distribution of void sizes included in the ring for one of the three realizations used in the simulations (solid blue line), is compared with the XCT measurements (black columns) and the Log-normal distribution fitted to the experiments (red solid line). The average number of voids and the corresponding standard deviation, in a quarter of the ring, for the three realizations that we have generated per sample, and for the 12 microstructures investigated, are shown in Table 2. The maximum number of voids, 34413 ± 120, corresponds to the microstructure Al3XY, and the minimum, 18 ± 2, to SS0.5Z. On the other hand, recall that our goal is to determine the influence of the porous microstructure in the necking and fragmentation patterns, providing new insights into the role of defects on dynamic localization and fracture, rather than developing an analysis on the influence of microstructure on the mechanical behavior of the specific materials considered.

The ring models were discretized using C3D4 general purpose tetrahedral elements (ABAQUS/Explicit, 2016). This type of element enables to describe the complex geometry of the porous media, as it is pictured in Fig. 13(b). Generally, as the number of voids increases, and the void size decreases, more elements are required to describe accurately the porous microstructure and the shape of the voids. In fact, for the microstructure Al3XY, which has the greater number of voids, we modeled only an eight of the ring to bound the number of elements in the finite element mesh. Specifically, using an average element size of 15 μm, the ring expansion models for the 12 microstructures investigated contain the number of elements reported in Table 2, ranging between 2.7 millions for the microstructure SS5Z and 18.9 for Al3Z. No specific element size has been used to seed the voids, instead,

each meridian of the voids was discretized with at least 5 elements, i.e., the number of elements surrounding the voids depends on the size of the void. For example, for a pore with diameter of 10 μm, the element size was $\approx$ 2 μm. The calculations were performed using a workstation with 24 CPUs with the following features: Intel Xeon Gold 6128 @ 3.4 GHz. The computational cost of each simulation shown in this paper ranged between 2 and 12 days, depending on the loading velocity and the microstructure considered, using simultaneously the 24 CPUs of the workstation indicated before.

	Al3Z	Al3XY	Al0.5Z	Al0.5XY	SS5Z	SS5XY	SS0.5Z	SS0.5XY	Ti0.5Z	Ti0.5XY	INC1Z	INC1XY
Voids	17377 ± 55	34413 ± 120	4748 ± 42	3997 ± 41	89 ± 4	76 ± 1	18 ± 2	186 ± 18	88 ± 3	26 ± 3	707 ± 26	1956 ± 32
Elements	18.9	14.1	9.1	9.1	2.7	5.8	5.7	5.9	5.9	5.8	4.0	8.3

Table 2: Average number of voids and corresponding standard deviation (Voids), and millions of elements (Elements) in the ring expansion finite element models developed in ABAQUS/Explicit (2016) for the 12 microstructures investigated.

4. Analysis and results: multiple necking

In this section, we investigate the influence of the porous microstructure on the multiple necking pattern that emerges around the circumference of the ring at large strains. We have performed ring expansion calculations for the 12 microstructures investigated (corresponding to the 12 samples analyzed), and for the 3 realizations of void size and position distribution that we have created per microstructure (R1, R2, R3). The material behavior is modeled using isotropic linear elasticity, with Young modulus $E = 200$ GPa and Poisson's ratio $\nu = 0.3$, and von Mises plasticity with constant yield stress $\sigma_y = 500$ MPa (i.e., the material is considered elastic perfectly-plastic). The initial material density is $\rho = 7800$ kg/m^3. The advantage of using this idealized constitutive modeling is that the formation and development of the necking pattern is solely controlled by inertia, stress multiaxiality (i.e. triaxiality) and porous microstructure, which facilitates the interpretation of results. In addition, considering that the material is elastic perfectly-plastic favors early necking formation, reducing mesh distortion problems. Recall that the objective of this paper is to determine the effect of porous microstructure on dynamic localization and fragmentation, and we do not pay attention to the specific mechanical response of the additively manufactured materials from which the microstructures are taken (this is left for a future work). In this regard, the reader is referred to the works of Li et al. (2020), Li et al. (2019), Tancogne-Dejean et al. (2016) and Ghorbanpour et al. (2020), among others, to obtain detailed information on the actual elastic/plastic behavior of additively manufactured $AlSi_{10}Mg$, stainless steel 316L, Ti_6Al_4V and Inconel 718L, respectively. Moreover, notice that inertia effects can be quantified with the dimensionless number $\hat{H}^{-1} = \sqrt{\frac{\rho h^2 \dot{\varepsilon}_0^2}{4\sigma_y}}$ which is derived from the balance of linear momentum (Zhou et al., 2006). For the calculations performed in this work (see Section 3), $\hat{H}^{-1}$ varies from 0.0033 for $V_r = 50$ m/s to 0.033 for $V_r = 500$ m/s. Note that, due to the stabilizing role of inertia (Vaz-Romero et al., 2017), the plastic strain outside the necks, after the necking pattern is formed, is generally above 3% in the calculations performed in this section for $V_r = 50$ m/s (in absence of inertia, a rate-independent material with no strain hardening develops instantaneous necking localization), increasing up to 25% for the greatest loading velocities investigated. In future works, we should perform calculations with specimens with greater cross-section to boost the effect of inertia (the relatively small cross-section samples investigated impose a limitation to the effect of inertia on the localization and fragmentation processes). Moreover, note that the large number of microstructures investigated makes impossible to show necking patterns and neck size distributions for all the simulations performed in this work. The idea is to display results that provide a general overview of the influence of porous microstructure in the necking pattern, and to compare microstructures with different void volume fractions, maximum pore diameters and average pore sizes.

AKI

4.1. The role of porous microstructure

Fig. 14 shows the normalized effective plastic strain $\hat{\bar{\varepsilon}}^p$ versus the normalized outer perimeter of the quarter ring $\hat{P} = \frac{2\theta}{\pi}$ (in the case of Al3XY it is one eight of the ring $\hat{P} = \frac{4\theta}{\pi}$), hereinafter also referred to as normalized radial angle, for the four microstructures corresponding to aluminium alloy $AlSi_{10}Mg$: (a) Al3Z, (b) Al3XY (c) Al0.5Z and (d) Al0.5XY. These are the microstructures with greater void volume fraction, see Table 1 (only INC1XY has comparable amount of porosity). The imposed loading velocity is $V_r = 250$ m/s, which corresponds to $\dot{\varepsilon}_0 = 16666$ s^{-1} and $\hat{H}^{-1} = 0.0165$. We compare the results obtained with the 3 realizations that we have generated per microstructure, where the black, red and green curves correspond to R1, R2 and R3, respectively. Recall that the three realizations (R1, R2, R3) provide different spatial and size distributions of the voids. The normalized effective plastic strain is defined as $\hat{\bar{\varepsilon}}^p = \frac{\bar{\varepsilon}^p}{\bar{\varepsilon}^p_b}$, where $\bar{\varepsilon}^p$ is the von Mises effective plastic strain measured in the outer surface of the specimen and $\bar{\varepsilon}^p_b = \ln\left(\frac{R_{out}+V_r t}{R_{out}}\right)$ approximates the background effective strain in the ring, where t is the loading time. The background effective strain corresponds to the fundamental/homogeneous solution of the problem (Vaz-Romero et al., 2017). Hence, before the localization process starts, the normalized effective plastic strain is ≈ 1. The $\hat{\bar{\varepsilon}}^p - \hat{P}$ curves display a succession of peaks and valleys. Similarly to N'souglo et al. (2018) and Vaz-Romero et al. (2017), we consider that necks are all the excursions of strain that meet the condition $\hat{\bar{\varepsilon}}^p = 1.1$ when the maximum value of $\hat{\bar{\varepsilon}}^p$ reaches ≈ 2. The necking criterion has been chosen so that the necking pattern is generally fully formed (i.e. no new necks are formed with the continuation of the loading process), yet the strains are not so large that the finite element grid becomes excessively distorted. The idea is to use a criterion for the identification of the necks such that the plastic strain is localized in the necked sections, and the portions of the ring outside the necked sections are unloaded. The ring expansion finite element calculations performed by Marvi-Mashhadi and Rodríguez-Martínez (2020) for rings with random distributions of geometric imperfections showed that the number of necks recorded is generally not very sensitive to the precise cut-off values of $\hat{\bar{\varepsilon}}^p$ used in the necking criterion. Note that the results shown in Fig. 14 correspond to the loading time for which the maximum value of $\hat{\bar{\varepsilon}}^p$ reaches ≈ 2, i.e. to the loading time for which the necking condition is met, hereinafter also referred to as necking time t_{neck}.

The number of necks N varies between 10 and 13 for Al3Z, Al0.5Z and Al0.5XY. In the case of Al3XY, the number of necks is about half, either 5 or 6, depending on the realization, because the calculations for this microstructure were performed modeling an eighth instead of a quarter of the ring, as stated in Section 3. Moreover, the necking time is smaller for Al3Z and Al3XY, than for Al0.5Z and Al0.5XY, because increasing the initial void volume fraction and the maximum diameter of the voids favors early necking formation, see Table 1 (we will elaborate on this issue later in this section). Notice that the results obtained for the 3 realizations (R1, R2, R3), in terms of necking time t_{neck} and number of necks N, are similar (see also Tables 3 and 4). In contrast, for a

given microstructure, the specific location of the necks varies with the microstructural realization. This becomes apparent in the contours of effective plastic strain shown in Fig. 15 for the realizations R1 and R2 corresponding to the microstructure Al3Z which show that, while the necking condition is met at the same loading time, the position of the necks is different (notice that the necks are numbered). Note that there is no evidence that the planes free of voids generated at the intersection of the 24 packed configurations used to build the ring lead to any specific necking pattern in the simulations, see Section 3. The color coding of the isocontours is such that effective plastic strains ranging from 0.1 to 0.35 correlate with a color scale that goes from blue to red. Effective plastic strains below 0.1 remain blue and above 0.35 remain red. The average value of the effective plastic strain outside the necks is $\approx 7\%$. The isocontours, which correspond to a cut view of the ring for the plane $Z = 0$, bring out the distribution of voids in the specimen. Note that the distance between pores varies from pore to pore. Note also that the pores inside the necked sections are elongated, while those located outside the necks remain nearly spherical.

Fig. 16 displays the $\hat{\bar{\varepsilon}}^p - \hat{P}$ curves for the 4 microstructures corresponding to stainless steel 316L: (a) SS5Z, (b) SS5XY, (c) SS0.5Z and (d) SS0.5XY. These microstructures display large variation in the maximum pore size, ranging from 25.90 μm for SS0.5Z to 100 μm for SS5Z, see Table 1. The results correspond to the necking time and the imposed velocity is $V_r = 250$ m/s. The comparison of the 3 realizations that we have generated per microstructure shows that the number of necks and the necking time hardly change with R1, R2 and R3 (see also Tables 3 and 4). In contrast, the number of necks varies between the different microstructures from 9 to 14, with the smaller number of necks and the smaller necking time corresponding to the microstructure SS5Z, which has the greatest void volume fraction and contains the biggest voids, see Table 1. The contours of effective plastic strain for SS5Z and realization R1 shown in Fig. 17 display two big pores acting as triggers for the localization of plastic deformation and the formation of early necks. The color coding of the isocontours is such that effective plastic strains ranging from 0.05 to 0.35 correlate with a color scale that goes from blue to red. Effective plastic strains below 0.05 remain blue and above 0.35 remain red. The microstructure SS5Z also displays the most irregular necking pattern, so that the two necks nucleated from the two big pores are significantly more developed than the others (numbers 6 and 8 in the case of R1, which corresponds to the black curve in Fig. 16(a)), leading to long neck-free segments (from $0.6 \lesssim \hat{P} \leq 1$ in the case of R1, see Fig. 16(a)).

Fig. 16 also pictures the initial void volume fraction VF (%) along the normalized radial angle $\hat{P}$ for realization R1 and the four microstructures considered (grey dashed lines). The void volume fraction is calculated in segments whose length being one hundredth part of the total perimeter of the ring. The results reveal that the more developed

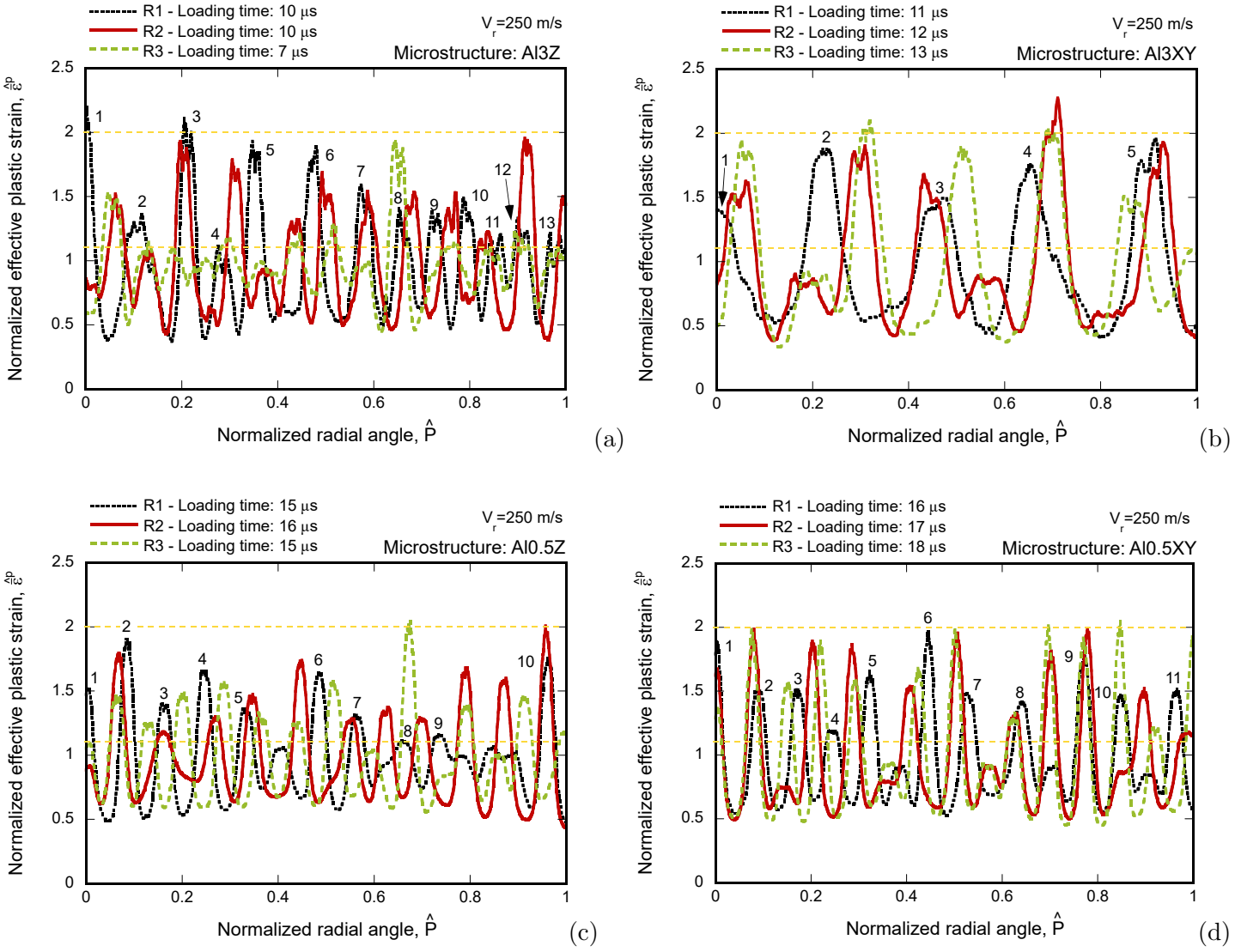

Figure 14: Normalized effective plastic strain $\hat{\bar{\varepsilon}}^p$ versus normalized outer perimeter of the ring $\hat{P}$ for microstructures: (a) Al3Z, (b) Al3XY, (c) Al0.5Z and (d) Al0.5XY. Results are shown for 3 realizations of void size and position distribution: R1, R2 and R3. Loading velocity $V_r = 250$ m/s. The loading time is taken when the necking condition is met. Note that the necks corresponding to the realization R1 are numbered. The horizontal yellow dashed lines correspond to $\hat{\bar{\varepsilon}}^p = 1.1$ and $\hat{\bar{\varepsilon}}^p = 2$. For interpretation of the references to color in this figure, the reader is referred to the web version of this article.

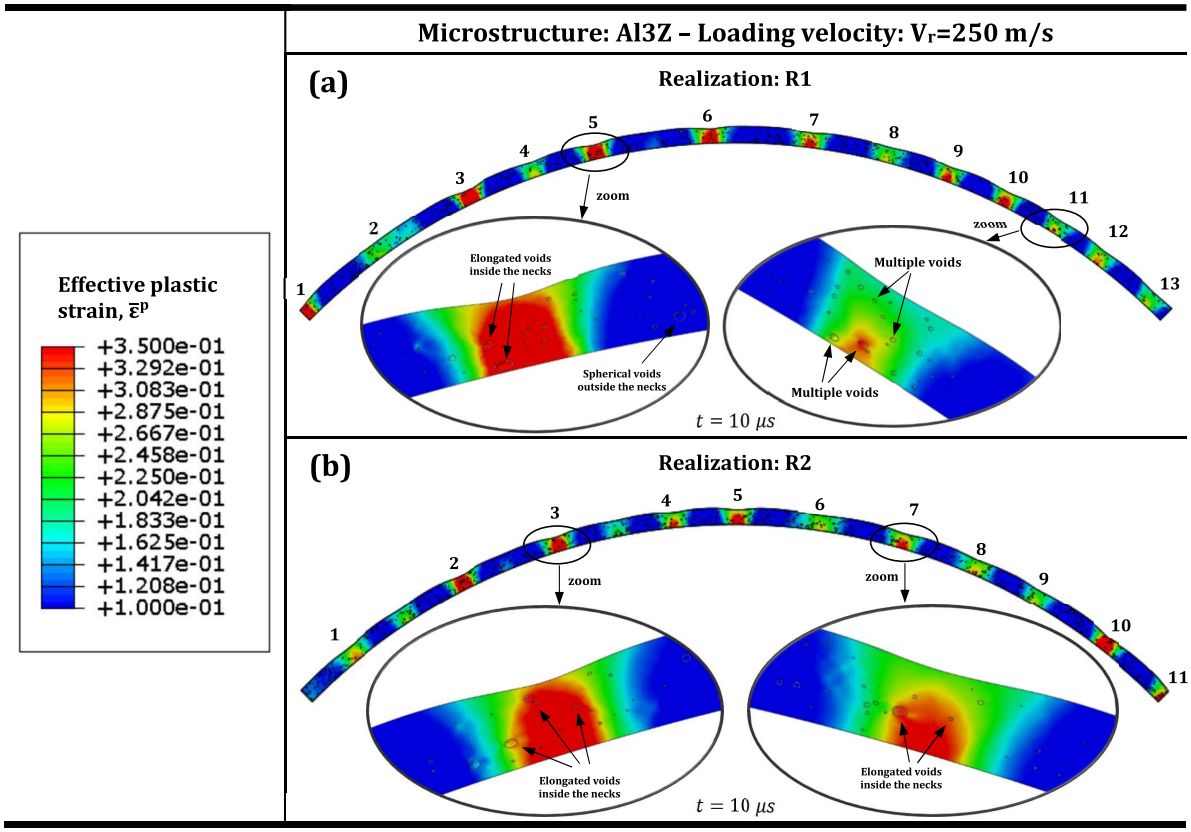

Figure 15: Contours of effective plastic strain $\bar{\varepsilon}^p$ for microstructure Al3Z. Loading velocity V_r = 250 m/s. Cut view of the ring corresponding to the plane $Z = 0$. (a) Realization R1. Loading time t = 10 μs. (b) Realization R2. Loading time t = 10 μs. For interpretation of the references to color in this figure, the reader is referred to the web version of this article.

necks for the four microstructures are nucleated at the locations with greater initial void volume fraction (segments with larger pores, or pore clusters). However, the location of many other necks does not seem to find a correlation with the porous microstructure. This suggests that the final necking pattern results from the competition between inertia and porous microstructure. For the microstructure SS0.5Z, for which the initial void volume fraction is the lowest and the maximum pores size is the smallest, the influence of porous microstructure seems to be less. As mentioned before, in future works we should perform calculations with specimens with greater cross-section to boost inertia effects and further check this conclusion.

The influence of the microstructure on the distribution of neck spacings is further illustrated in Fig. 18, which shows histograms with the number of necks N_{neck} as a function of the normalized Lagrangian neck spacing $\hat{L}_{neck} = \frac{L_{neck}}{h}$ for: (a) SS5Z, (b) SS5XY, (c) SS0.5Z and (d) SS0.5XY. The Lagrangian neck spacing L_{neck} is the distance between the central sections of two consecutive necks referred to the undeformed configuration. The idea is to identify the characteristic distribution of neck sizes for each microstructure, so that the more realizations we include in the histograms, the more representative the results are for that given velocity and microstructure. However, as mentioned before, the computational cost of the calculations is high, and the number of realizations per microstructure is limited to three, i.e., the results correspond to the three realizations we have performed per microstructure, R1, R2 and R3, which are represented by black, red and green blocks, respectively. The height of a colored block within a bar of the histogram marks the number of necks with fixed $\hat{L}_{neck}$ for a given realization. The greater scatter in the distribution of neck spacings corresponds to SS5Z, for which the normalized Lagrangian neck spacing varies between 3.16 and 9.74, with an average value of 4.72. The smaller scatter corresponds to the microstructure SS0.5Z, which has the smaller void volume fraction and the smaller value of d_{max}, see Table 1. For this microstructure, $\hat{L}_{neck}$ varies between 2.88 and 5.75, with an average value of 3.66, suggesting that decreasing the void volume fraction and the maximum size of the voids favors the formation of more regularly spaced necks.

Tables 3 and 4 compile the number of necks and the necking time, respectively, for the 12 microstructures investigated (corresponding to the 12 samples analyzed), and for the 3 realizations that we have created for each microstructure, R1, R2 and R3. The imposed loading velocity is $V_r = 250$ m/s (as in Figs. 14-18). These results are plotted in Fig. 19 with respect to: (a) the initial void volume fraction VF (%), (b) the maximum void diameter d_{max} and (c) the average void size μ. Recall that the values of VF (%), d_{max} and μ corresponding to each microstructure are given in Table 1.

Fig. 19(a) illustrates that both number of necks N_{neck} and necking time t_{neck} decrease with the initial void

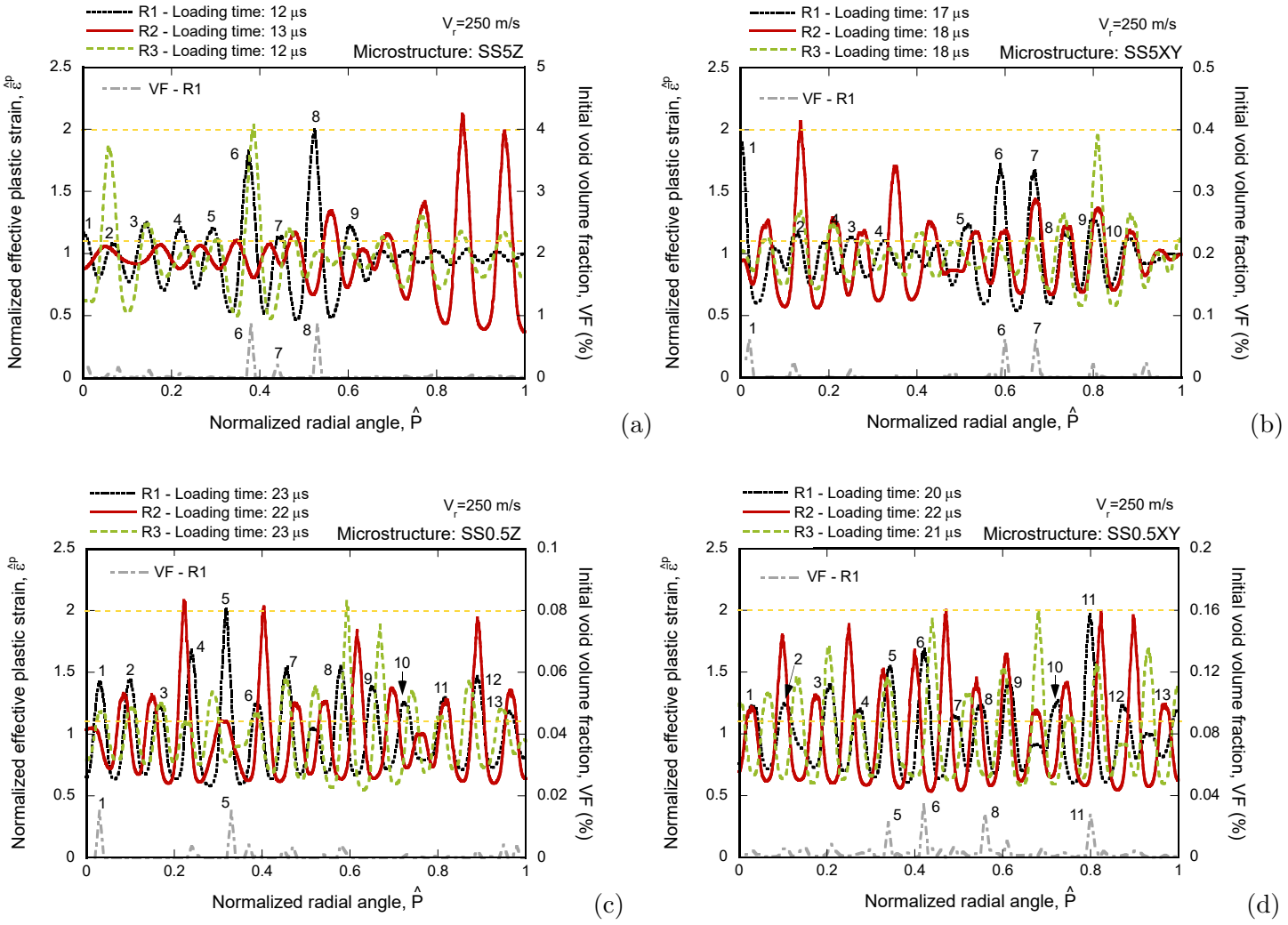

Figure 16: Normalized effective plastic strain $\hat{\bar{\varepsilon}}^p$ and initial void volume fraction VF (%) versus normalized outer perimeter of the ring $\hat{P}$ for microstructures: (a) SS5Z, (b) SS5XY, (c) SS0.5Z and (d) SS0.5XY. Results for the effective plastic strain are shown for 3 realizations of void size and position distribution: R1, R2 and R3. Results for the initial void volume fraction correspond to R1. Loading velocity $V_r = 250$ m/s. The loading time for the results of the effective plastic strain corresponds to the necking condition. Note that the necks corresponding to the realization R1 are numbered. The horizontal yellow dashed lines correspond to $\hat{\bar{\varepsilon}}^p = 1.1$ and $\hat{\bar{\varepsilon}}^p = 2$. For interpretation of the references to color in this figure, the reader is referred to the web version of this article.

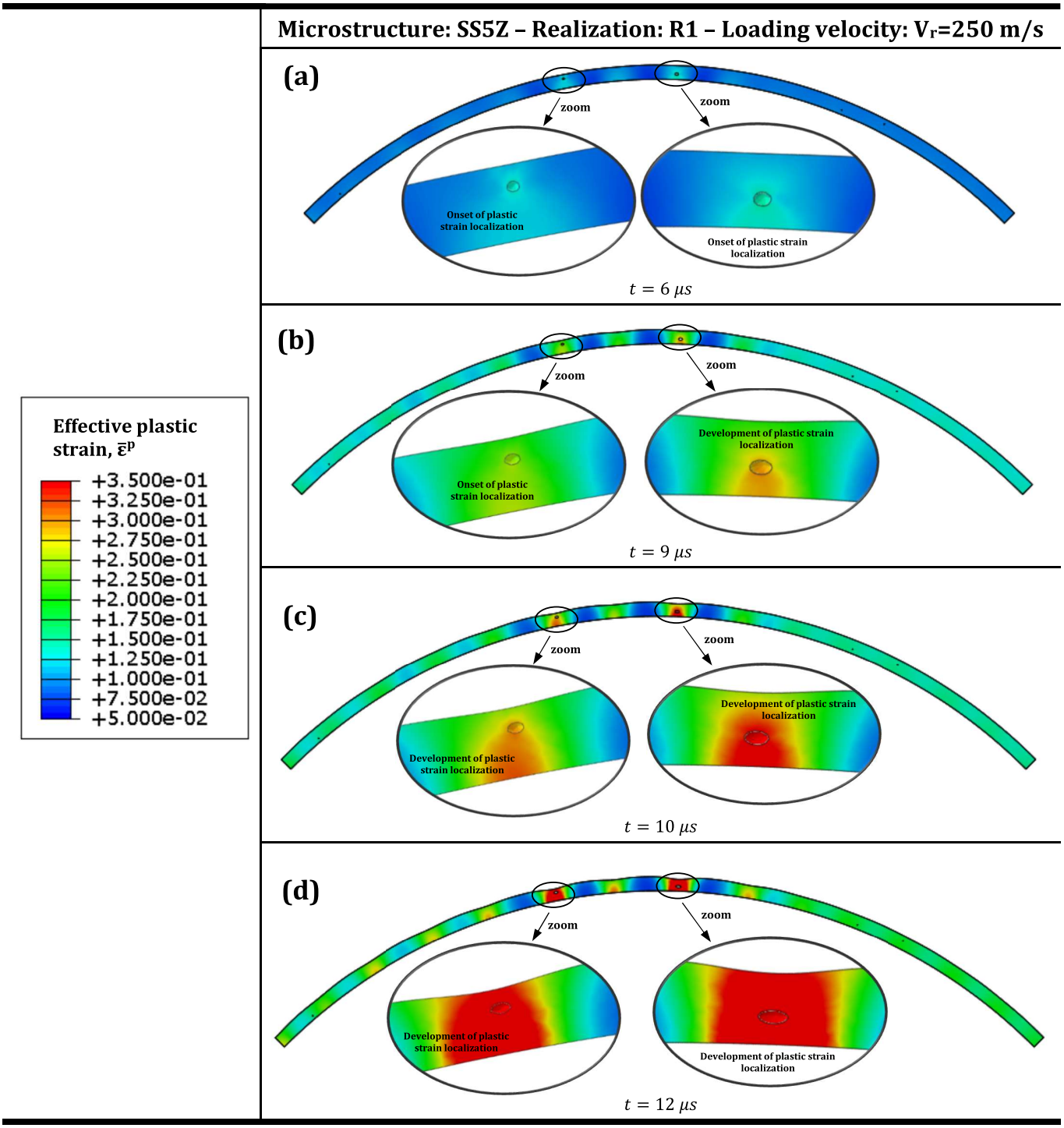

Figure 17: Contours of effective plastic strain $\bar{\varepsilon}^p$ for microstructure SS5Z. Realization R1. Cut view of the ring corresponding to the plane $Z = 0$. Loading velocity $V_r = 250$ m/s. Loading time: (a) $t = 6$ μs, (b) $t = 9$ μs, (c) $t = 10$ μs and (d) $t = 12$ μs. For interpretation of the references to color in this figure, the reader is referred to the web version of this article.

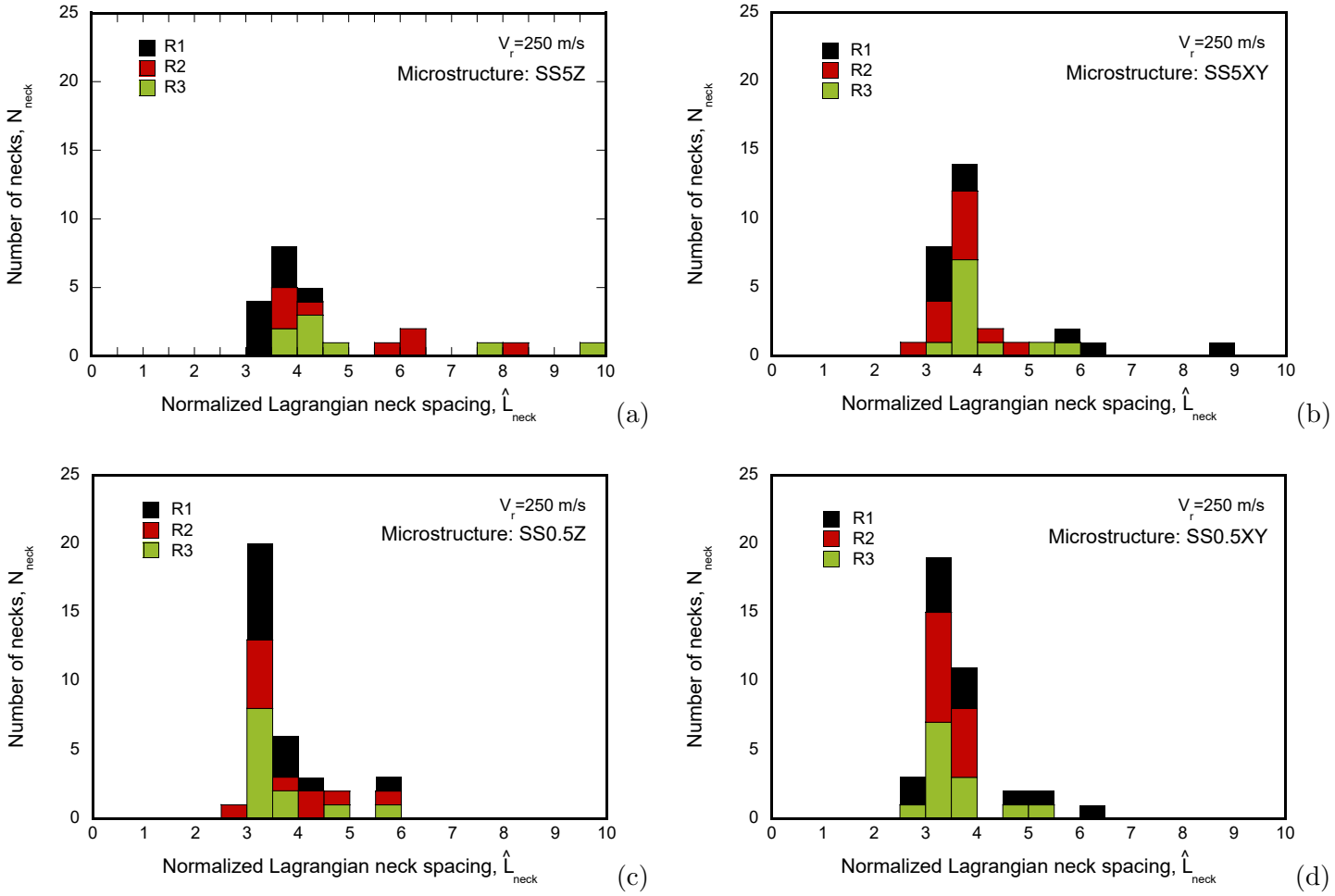

Figure 18: Histograms showing the number of necks N_{neck} as a function of the normalized Lagrangian neck size $\hat{L}_{neck} = \frac{L_{neck}}{h}$ for microstructures: (a) SS5Z, (b) SS5XY, (c) SS0.5Z and (d) SS0.5XY. Results are shown for 3 realizations of void size and position distribution: R1, R2 and R3. Loading velocity $V_r = 250$ m/s. For interpretation of the references to color in this figure, the reader is referred to the web version of this article.

volume fraction VF (%) (which is plotted in log scale). Note that the drop of the necking time is significantly more pronounced. Based on the logarithmic functions used to fit the finite element results, the necking time decreases from $\approx$ 22 μs for $f = 0.0007\%$ up to $\approx$ 10 μs for $f = 2.17\%$ (120% drop), while the number of necks varies between ≈ 12 and ≈ 10. It becomes apparent that porosity promotes necking localization, leading to a significant decrease of the specimen ductility for this expansion velocity (250 m/s) and this range of initial void volume fractions. Moreover, notice that an increase of three orders of magnitude in the initial void volume fraction *only* reduces the number of necks by 20%. The necking time for the microstructures SS5XY, Al0.5XY and INC1XY is similar, ranging between 16 μs and 18 μs for the three realizations performed per microstructure, see Table 4. The corresponding void volume fractions are quite different, 0.0025%, 0.0203% and 0.14%, while the maximum diameter of the voids is similar, 41.40 μm, 45.52 μm and 41.24 μm, respectively. These results suggest that, for this loading velocity, the maximum void diameter has an important influence on the necking time. In fact, Fig. 19(b) shows that increasing the maximum void diameter d_{max} also leads to a decrease of both the number of necks N_{neck} and the necking time t_{neck}. Note that microstructures with similar maximum void size have different void volume fraction (e.g. see Al0.5XY, SS5XY and INC1XY in Table 1). The finite element results are fitted with linear functions which predict that increasing d_{max} from 25.9 μm to 110.53 μm leads to a decrease in the number of necks and the necking time of 20% and 120%, respectively. Note that for microstructures with similar void volume fraction, like Al0.5Z, Al0.5XY, INC1Z for which VF ranges between 0.13% and 0.14%, the lower necking times are obtained for INC1Z, which contains the voids with greater diameter. This reinforces the idea that big pores are preferential locations for the inception of early necks (see Fig. 17). Moreover, these results also suggest that the spacing between necks is less sensitive to the porous microstructure than the critical strain triggering localization. In addition, notice that the scatter in the results is more important for the necking time than for the necking strain. Fig. 19(c) brings out that, while the number of necks N_{neck} decreases with μ (based on the linear function used to fit the finite element results), there does not seem to be any connection between the necking time t_{neck} and the average void size. Note that the maximum necking time is obtained for $\mu = 17.30$ μm, which corresponds to Ti0.5XY, and the minimum for $\mu = 11.31$ μm, which corresponds to Al3Z.

To the authors' knowledge, these results provide the first correlations ever reported for the ring expansion problem between material porous microstructure, number of necks and loading time for which the necks are formed, including individual identification of the roles played by initial void volume fraction, maximum void diameter and average void size. The maximum void diameter seems to be the main microstructural feature controlling the necking pattern, however, obtaining definite conclusions requires additional efforts which are left for a future work (e.g. this analysis should be repeated for other expanding velocities).

Number of necks - $\mathbf{V_r = 250}$ m/s			
Microstructure	**R1**	**R2**	**R3**
Al3Z	13	11	10
Al3XY	5	5	6
Al0.5Z	10	11	12
Al0.5XY	11	11	13
SS5Z	9	9	9
SS5XY	10	12	12
SS0.5Z	13	12	13
SS0.5XY	13	14	14
Ti0.5Z	13	12	12
Ti0.5XY	13	14	13
INC1Z	11	10	13
INC1XY	13	12	11

Table 3: Number of necks N_{neck} obtained for the 12 microstructures investigated in this work: Al3Z, Al3XY, Al0.5Z, Al0.5XY, SS5Z, SS5XY, SS0.5Z, SS0.5XY, Ti0.5Z, Ti0.5XY, INC1Z and INC1XY. Results are shown for the 3 realizations $(\mathrm{R1}, \mathrm{R2}, \mathrm{R3})$ that we have generated per microstructure. The loading velocity is $V_r = 250$ m/s.

Necking time (μs) - $\mathbf{V_r = 250}$ m/s			
Microstructure	**R1**	**R2**	**R3**
Al3Z	10	10	7
Al3XY	11	12	13
Al0.5Z	15	16	15
Al0.5XY	16	17	18
SS5Z	12	13	12
SS5XY	17	18	18
SS0.5Z	23	22	23
SS0.5XY	20	22	21
Ti0.5Z	19	21	20
Ti0.5XY	22	22	23
INC1Z	13	12	14
INC1XY	17	16	17

Table 4: Necking time t_{neck} obtained for the 12 microstructures investigated in this work: Al3Z, Al3XY, Al0.5Z, Al0.5XY, SS5Z, SS5XY, SS0.5Z, SS0.5XY, Ti0.5Z, Ti0.5XY, INC1Z and INC1XY. Results are shown for the 3 realizations $(\mathrm{R1}, \mathrm{R2}, \mathrm{R3})$ that we have generated per microstructure. The loading velocity is $V_r = 250$ m/s.

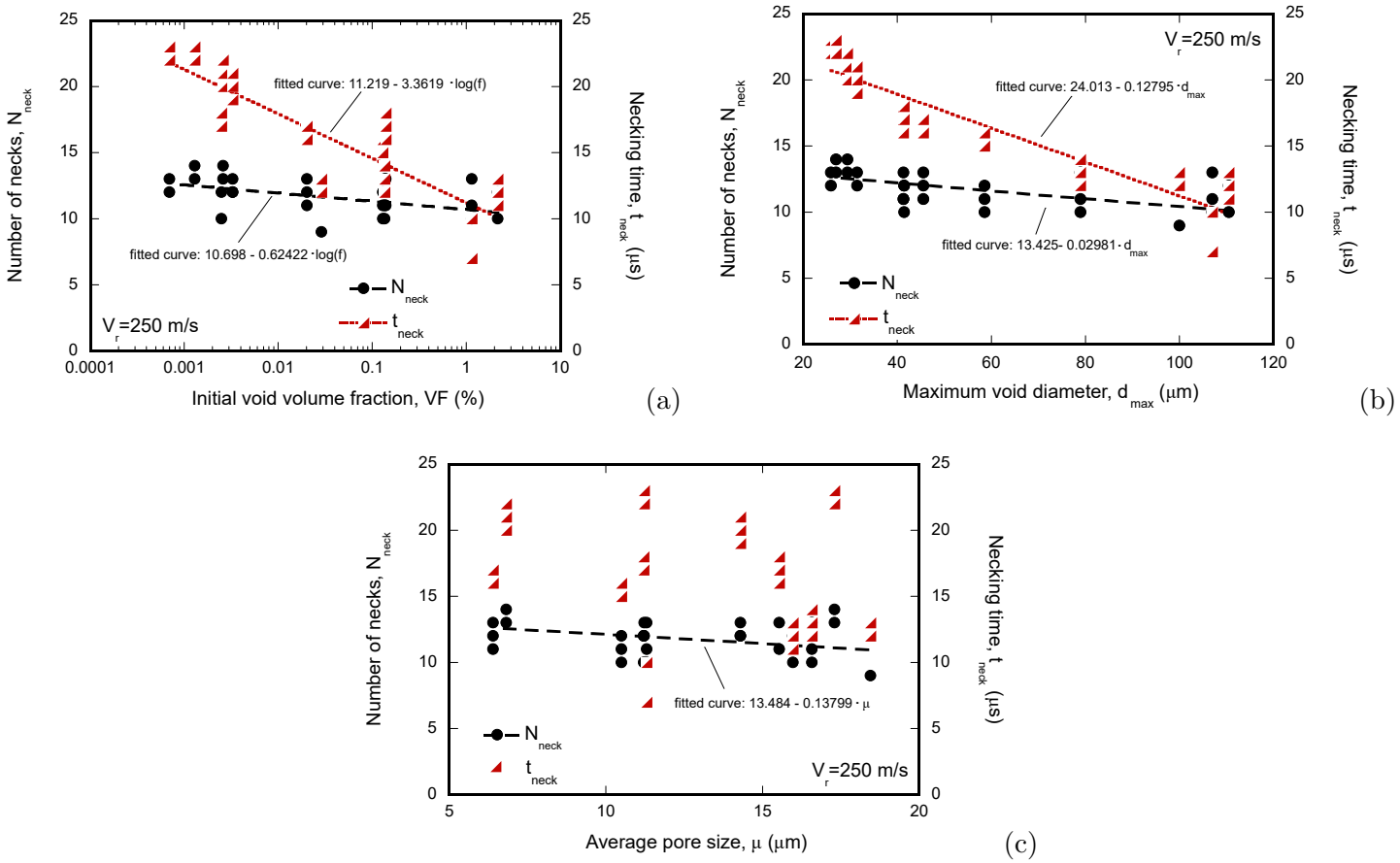

Figure 19: Number of necks N_{neck} and necking time t_{neck} versus: (a) initial void volume fraction VF (%), (b) maximum void diameter d_{max} and (c) average void size μ. Results are shown for the 12 microstructures investigated in this work and the 3 realizations (R1, R2, R3) that we have generated per microstructure. The loading velocity is $V_r = 250$ m/s.

4.2. The role of expansion velocity

Fig. 20 shows the normalized effective plastic strain $\hat{\bar{\varepsilon}}^p$ versus the normalized outer perimeter of the ring $\hat{P}$, for: (a) Al3Z (b) SS0.5Z and (c) INC1Z. The three porous microstructures display large differences for the void volume fraction and the maximum void diameter, see Table 1. The comparison between the results obtained for three different loading velocities $V_r = 50$, 250 and 500 m/s (the corresponding values of $\hat{H}^{-1}$ are 0.0033, 0.0165 and 0.033, respectively) is presented. The results correspond to the necking time, and the associated background strain is indicated in the plots. The calculations correspond to realization R1.

The number of necks increases with the applied velocity. Zhang and Ravi-Chandar (2006, 2008) attributed this behavior to the fact that for the lower expansion rates, the release waves that emanate from the necks that form earlier have the time to unload larger segments of the specimen; contrary to what happens at higher expansion rate, when the time for the released waves to travel and unload the specimen is less, allowing for the nucleation of more necks closer together. An alternative explanation for the increase in the number of necks with the expansion rate, that stems from the works of Fressengeas and Molinari (1994), Mercier and Molinari (2004), Rodríguez-Martínez et al. (2013a) and N'souglo et al. (2020), among others, is that inertia stabilizes material behavior, delays localization and promotes the development of preferential necking wavelengths that lead to the formation of additional (smaller) necks as the strain rate (loading velocity) increases. The stabilizing effect of inertia is responsible for the increase of the background strain corresponding to the necking time with the expansion velocity.

The calculations performed with the microstructure Al3Z, Fig. 20(a), predict that the number of necks is 9, 13 and 14 for 50, 250 and 500 m/s, respectively. Some necks repeatedly nucleate at the same location for the three velocities, numbers $1-3$, $4-6$ and 9, suggesting that these are triggered by the porous microstructure (most likely by big pores or pore clusters). In contrast, as the expansion velocity increases, localization is delayed and additional necks are nucleated at different positions of the ring. The blue arrows indicate necks that emerge for 500 m/s at locations that were neck-free for 50 m/s. Moreover, the split up of long necks into two at higher velocities also leads to additional necks for 500 m/s which are indicated with orange arrows. Attending to the results presented in Figs. 14 and 5 of Rodríguez-Martínez et al. (2013a) and Rodríguez-Martínez et al. (2017), respectively, the split up of long necks into smaller ones can be attributed to inertia, which promotes the development of smaller necking wavelengths as the loading rate and the material deformation increase. Nevertheless, it is difficult to attribute a single origin to any neck of the pattern, and it could be the case that the microstructure also contributes –probably less than inertia– to the formation of these additional necks that develop at high strain rates.

For the microstructure SS0.5Z, Fig. 20(b), the localization pattern is formed by 10, 13 and 16 necks, for 50, 250 and 500 m/s, respectively. Necks 4, 5, 6 and 9 seem to be triggered by the porous microstructure since they are located in the same position for the three velocities investigated. The necks indicated with blue and orange

arrows, as in the case of the calculations shown in Fig. 20(a) for Al3Z, only appear at high expansion rate, and their nucleation seems to be favored by the increase of inertia with the loading velocity. Moreover, notice that, although neck number 4 is the first to meet the necking criterion for the three velocities, the level of development (peak strain) of the necks triggered by the microstructure, and of the necks that appear at higher expansion velocity, is generally similar. Note that the invariance of neck positions with applied velocity seems to be less pronounced for SS0.5Z than for the two microstructures shown in Figs. 20(a) and 20(c). This could be attributed to the fact that the maximum void diameter is smaller for SS0.5Z. The maximum void size seems to play the role of a weakest link, which interplays with the loading rate (inertia) to determine the necking time (as discussed in Section 4.1) and the position of some necks.

The calculations corresponding to the microstructure INC1Z predict that increasing the velocity from 50 m/s to 500 m/s leads to a variation in the number of necks that goes from 9 to 14, see Fig. 20(c). The isocontours of effective plastic strain $\bar{\varepsilon}^p$ shown in Fig. 21 illustrate the formation of additional necks with the increase of the loading rate in segments of the ring that were neck-free at lower expansion velocities. Note that the color coding of the isocontours is different for the three expansion velocities, so that the plastic strains inside the necks are greater as the loading rate increases. Outside the necks, the average plastic strain for 50 m/s, 250 m/s and 500 m/s is ≈ 0.014, 0.11 and 0.21, respectively (notice that the average plastic strain outside the necks does not match with the background strain, because the latter is calculated assuming that the strain distribution in the specimen is fully homogeneous until the necking condition is met). The isocontours correspond to a cut view of the ring for the plane $Z = 0$ (as in Fig. 15) so that they expose the distribution of voids inside the specimen. Notice that the voids in the necked zones, which are nearly spherical for 50 m/s because the localization starts for relatively low strains (0.014 as indicated before), become elongated as the expansion speed increases, because necking formation is delayed due to inertia. Moreover, notice that the loading time corresponding to the necking condition is smaller for the microstructure INC1Z than the microstructure SS0.5Z, and greater than for the microstructure Al3Z, for the three expansion velocities. These results bring out that the necking time decreases with the void volume fraction and with the maximum void diameter for any velocity within the range of expansion rates investigated in this work (recall that the values of VF(%) and d_{max} for the microstructure INC1Z are greater/smaller than for the microstructure SS0.5Z/Al3Z).

These results suggest that both porous microstructure and inertia play a role in the resulting necking patterns. While the microstructure seems to impose the nucleation of necks at specific locations (weak points) of the specimen for all the velocities investigated, inertia delays localization and favors the nucleation of additional necks at higher loading rates. As mentioned before, future works should consider specimens with greater cross-section to increase inertia effects and provide further insights into the interplay between inertia and porous microstrcture on necking

and fragmentation.

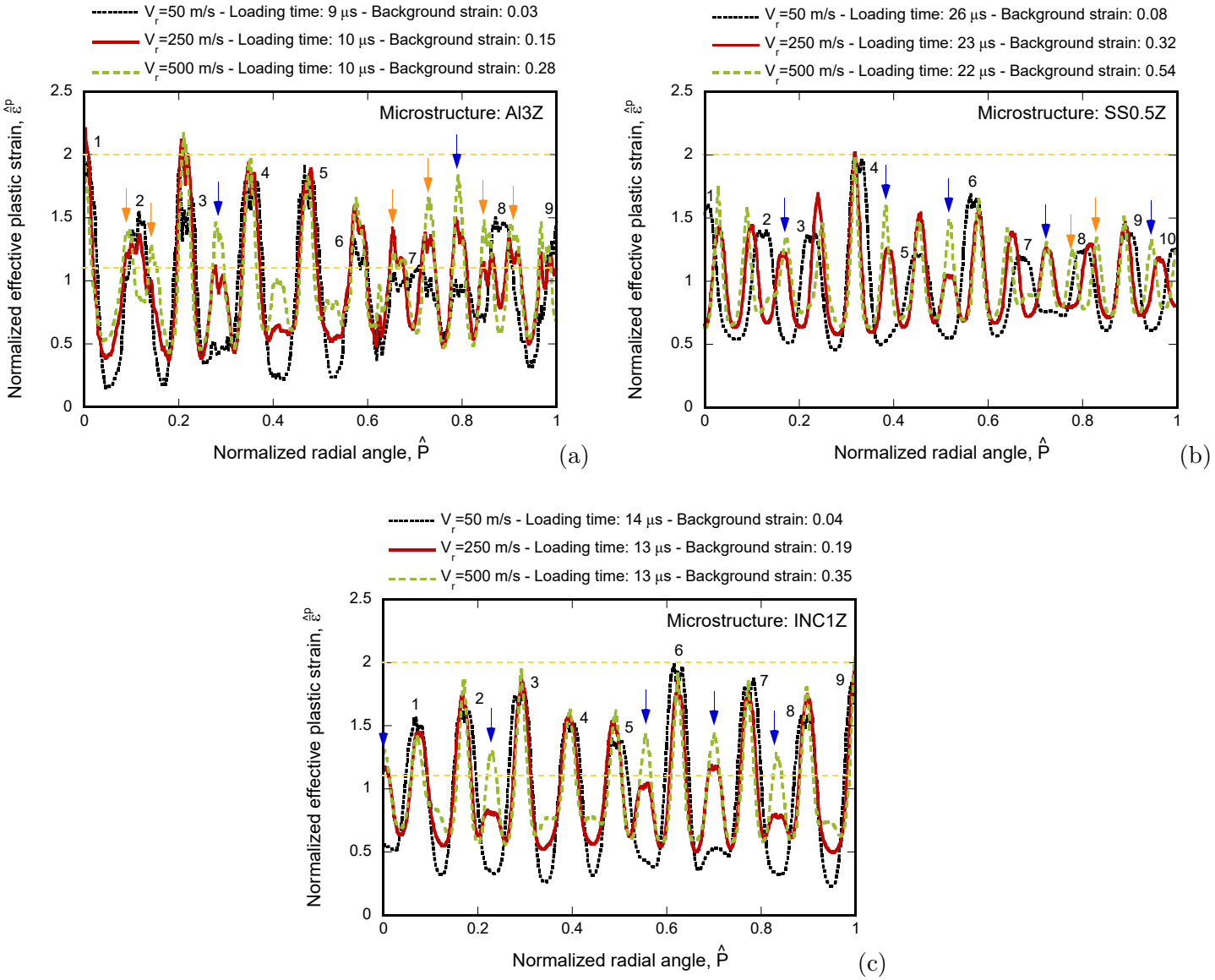

Figure 20: Normalized effective plastic strain $\hat{\varepsilon}^p$ versus normalized outer perimeter of the ring $\hat{P}$. Results are shown for three different loading velocities V_r: 50 m/s, 250 m/s and 500 m/s. (a) Microstructure: Al3Z. (b) Microstructure: SS0.5Z. (c) Microstructure: INC1Z. The calculations with the porous microstructures correspond to realization R1. The loading time is taken when the necking condition is met. The horizontal yellow dashed lines correspond to $\hat{\varepsilon}^p = 1.1$ and $\hat{\varepsilon}^p = 2$. For interpretation of the references to color in this figure, the reader is referred to the web version of this article.

Fig. 22 shows the evolution of the average normalized Lagrangian neck spacing $\hat{L}^{avg}_{neck}$ with the inertia parameter $\hat{H}^{-1}$ for finite element results obtained with the microstructures Al3Z, SS0.5Z and INC1Z. Note that using the inertia parameter instead of the strain rate or the expansion velocity to plot the evolution of the average normalized Lagrangian neck spacing enables to compare results obtained with specimens with different cross-section dimensions, and with materials displaying different initial density and yield stress. The average normalized Lagrangian neck spacing is defined as the ratio between the normalized outer perimeter of the quarter ring and the

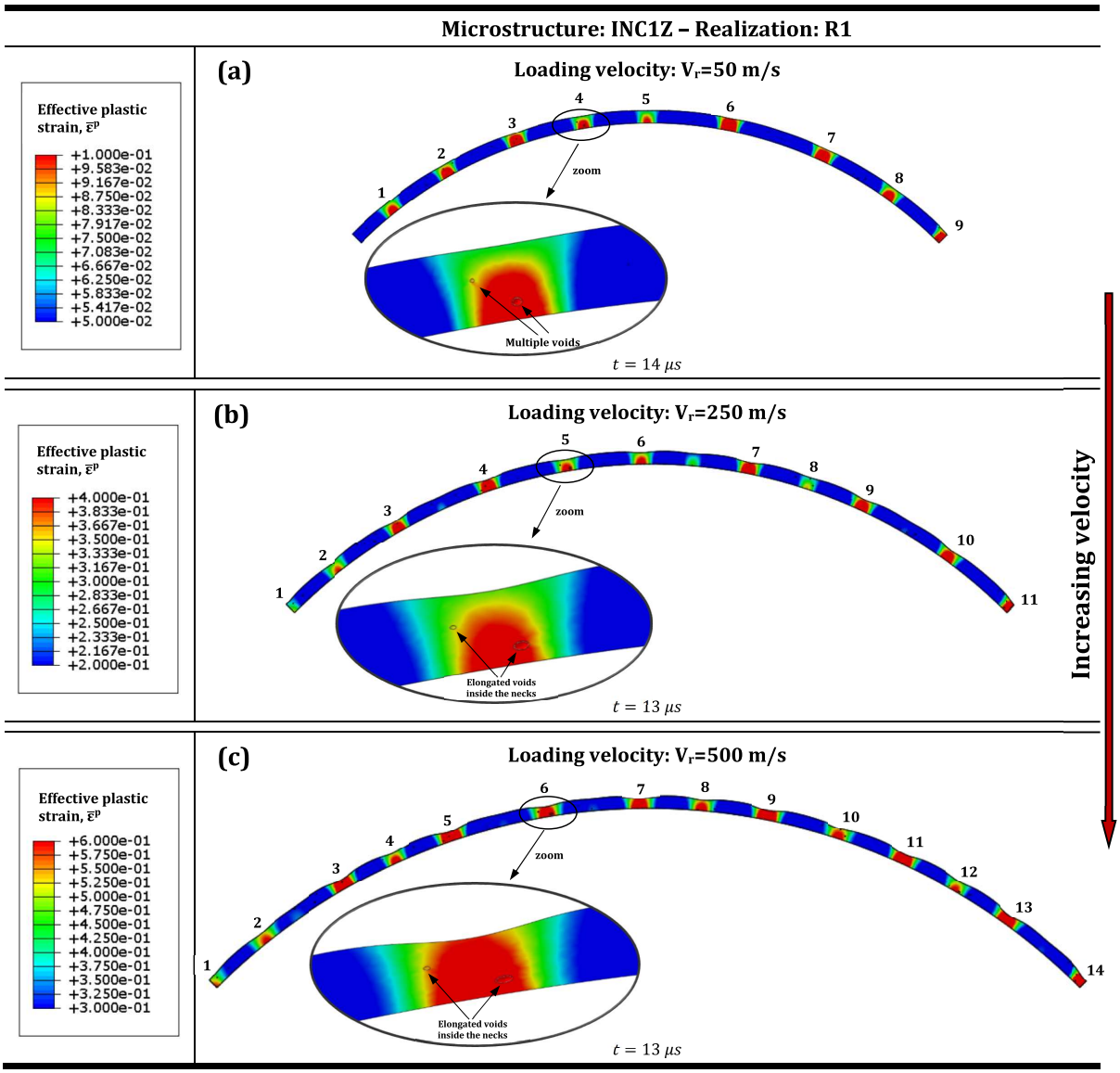

Figure 21: Contours of effective plastic strain $\bar{\varepsilon}^p$ for microstructure INC1Z. Realization R1. Cut view of the ring corresponding to the plane $Z = 0$. (a) Loading velocity $V_r = 50$ m/s. Loading time $t = 14$ μs. (b) Loading velocity $V_r = 250$ m/s. Loading time $t = 13$ μs. (c) Loading velocity $V_r = 500$ m/s. Loading time $t = 13$ μs.

number of necks $\hat{L}_{neck}^{avg} = \dfrac{\pi R_{ext}}{2hN_{neck}}$. A comparison with the finite element calculations performed by Guduru and Freund (2002), and with the finite element calculations and the linear stability analysis results reported by N'souglo et al. (2018) is presented. The results of Guduru and Freund (2002) and N'souglo et al. (2018) were obtained for bars with circular cross-section, subjected to dynamic stretching, with initial and boundary conditions consistent with the ring expansion problem, and modeled using Gurson plasticity with an initial void volume fraction of 0.01 (in the case of N'souglo et al. (2018)). Additional stability analysis results obtained with the analytical model of N'souglo et al. (2018) for the perfectly-plastic material are pictured. The yield stress is 500 MPa –recall that this is the value used in the finite element calculations presented in this section– and the initial void volume fraction is 0.0115 –which corresponds to the microstructure Al3Z–.

The finite element results obtained in this work are in quantitative agreement with the numerical simulations of Guduru and Freund (2002). On the other hand, the agreement with the stability analysis and with the numerical simulations obtained with the analytical and numerical models of N'souglo et al. (2018) is only qualitative, with the simulations performed in this work predicting greater values of $\hat{L}_{neck}^{avg}$ for the whole range of values of $\hat{H}^{-1}$. The differences are greater for the stability analysis performed with the perfectly-plastic material. While it is difficult to determine the specific reason for this disagreement, it may be attributed to the fact that the models of N'souglo et al. (2018) do not consider the actual microstructure of the material and neglect the shielding effect of the release waves that emanate from the voids, which may prevent the development of some necks. In addition, the formulation of the stability analysis is based on a series of simplifications, e.g., it does not take into account the elastic unloading arising after the nucleation of the necks –which may affect the necking pattern especially at lower strain rates–, and it assumes that the problem is 1D, using the Bridgman (1952) correction factor to account for the hydrostatic stresses that develop inside a necked section. In any case, all the results presented in Fig. 22 show that the average neck spacing decreases with the inertia parameter, the decrease being milder as $\hat{H}^{-1}$ increases.

5. Analysis and results: fragmentation

In this section, we investigate the influence of porosity in the fragmentation of the rings using the 12 microstructures considered in this work. We have performed calculations with the 3 realizations of void size and position distribution (R1, R2, R3) employed in Section 4 for selected microstructures: Ti0.5Z, Ti0.5XY, INC1Z and INC1XY. For all other microstructures, we have performed calculations with only R1 and/or R2 realizations due to the large computational cost of the simulations. The material behavior is modeled using isotropic linear elasticity and von Mises plasticity with associated flow rule, with yield stress evolving with the effective plastic strain $\bar{\varepsilon}^p$, the effective plastic strain rate $\dot{\bar{\varepsilon}}^p$ and the temperature T, according to the following power-law type relation:

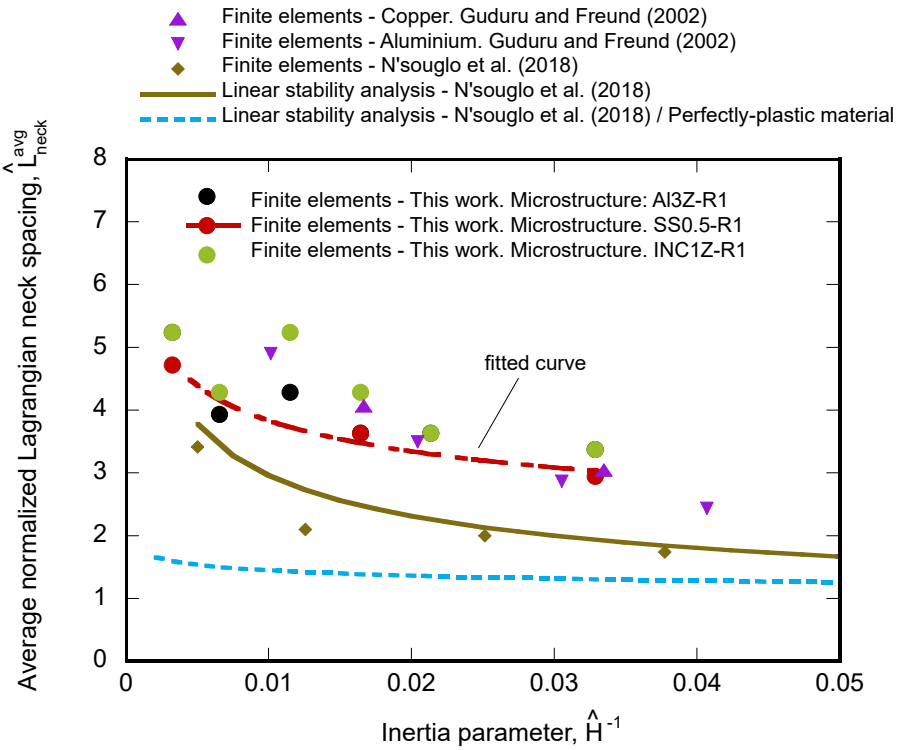

Figure 22: Average normalized Lagrangian neck spacing $\hat{L}_{neck}^{avg}$ versus inertia parameter $\hat{H}^{-1}$. Finite element results obtained in this work for the microstructures Al3Z, SS0.5Z and INC1Z. The calculations with the porous microstructures correspond to realization R1. Comparison with the finite element calculations performed by Guduru and Freund (2002) and with finite element calculations and linear stability analysis results computed with the numerical and analytical models developed by N'souglo et al. (2018). The finite element results obtained in this work with the microstructure SS0.5Z are fitted with the curve $\hat{L}_{neck}^{avg} = 1.548 \left(\frac{1}{\hat{H}}\right)^{-0.196}$.

$$\sigma_Y = \sigma_0 + \sigma_K \left(\bar{\varepsilon}^p\right)^n \left(\frac{\dot{\bar{\varepsilon}}^p}{\dot{\varepsilon}_{ref}}\right)^m \left(\frac{T}{T_{ref}}\right)^{-\mu} \tag{3}$$

where σ_0, σ_K, n, $\dot{\varepsilon}_{ref}$, m, T_{ref} and μ are material parameters. Moreover, assuming adiabatic conditions of deformation (no heat flux) and considering that plastic work is the only source of heating, the evolution of temperature is given by:

$$\dot{T} = \beta \frac{\bar{\sigma}\dot{\bar{\varepsilon}}^p}{\rho C_p} \tag{4}$$

where β is the Taylor-Quinney coefficient, ρ is the current material density and C_p is the specific heat. The values of the material parameters are given in Table 5, and they correspond to steel AISI 430 (Vaz-Romero et al., 2015). In Sections 5.1 and 5.2, we perform a comparison between the results obtained with this viscoplastic modeling, and the elastic perfectly-plastic material used in Section 4.

Symbol	**Property and units**	**Value**
ρ_0	Initial density (kg/m^3)	7740
C_p	Specific heat (J/kg K), Eq. (4)	460
E	Young modulus (GPa)	200
ν	Poisson's ratio	0.3
σ_0	Initial yield stress (MPa), Eq. (3)	175.67
σ_K	Hardening modulus (MPa), Eq. (3)	530.13
n	Strain hardening exponent, Eq. (3)	0.167
m	Strain rate sensitivity exponent, Eq. (3)	0.0118
$\dot{\varepsilon}_{ref}$	Reference strain rate (s^{-1}), Eq. (3)	0.01
μ	Temperature sensitivity exponent, Eq. (3)	0.51
T_{ref}	Reference temperature (K^{-1}), Eq. (3)	300
β	Taylor-Quinney coefficient, Eq. (4)	0.9

Table 5: *Values of the material parameters used in the finite element calculations as taken from Vaz-Romero et al. (2015).*

Material failure is accounted for in the finite element simulations using the element deletion technique available in ABAQUS/Explicit (2016). We consider that failure occurs when a critical value of the accumulated plastic strain, $\bar{\varepsilon}^p_f = 1$, is reached. This value was chosen because the necking pattern has fully developed for all the velocities and microstructures investigated, yet the strains are not so large that the finite element grid has become significantly deformed. We are aware that assuming a constant value for the critical failure strain is a crude assumption, since the failure strain of metallic materials is generally dependent on the stress state, the strain rate and the

temperature (Pandya et al., 2020; Habib et al., 2019; Khan and Liu, 2012). However, using this simple failure criterion facilitates the analysis and the interpretation of results. Moreover, note that the same failure criterion was used in the ring expansion fragmentation calculations performed by Rusinek and Zaera (2007), Zhang and Ravi-Chandar (2008) and Vaz-Romero et al. (2019).

5.1. The role of porous microstructure

Fig. 23 displays the evolution of the normalized effective plastic strain $\hat{\bar{\varepsilon}}^p$ versus the normalized radial angle $\hat{P}$ for microstructure Ti0.5Z. This microstructure displays low void volume fraction and relatively small maximum pore size, see Table 1, which is assumed to boost the effect of inertia in the necking and fragmentation processes. The results obtained for 3 realizations of void size and position distribution, R1, R2 and R3, are compared for the expansion velocity $V_r = 250$ m/s. The loading time is taken when the necking condition is met. The number of necks for the three realizations is 11, 9 and 11, respectively, with the specific location of the necked sections varying with the realization. Notice that the number of necks is smaller as compared to the simulations performed in Section 4 for the same microstructure with the elastic perfectly-plastic material, for which the number of necks was 13, 12 and 12, for R1, R2 and R3, respectively, see Table 3. On the other hand, the necking time is greater, see Table 4, most likely due the stabilizing role of strain hardening and strain rate hardening, which delay necking formation and increase specimen ductility (Hutchinson and Neale, 1977; Chung and Wagoner, 1988). These results bring out the effect of the constitutive behavior of the material in the necking pattern (this issue will be further discussed in Section 5.2).

The location of the fractures and the size of the fragments also depends on the realization of void size and position distribution. Fig. 24 shows contours of effective plastic strain $\bar{\varepsilon}^p$ for the same calculations presented in Fig. 23. The color coding of the isocontours is such that effective plastic strains ranging from 0.4 to 0.8 correlate with a color scale that goes from blue to red. Effective plastic strains below 0.4 remain blue and above 0.8 remain red. The loading time for the contour plots is taken 8 μs after the necking condition is met, so that the fragmentation process is completed (no additional fractures occur for greater loading times). There are 4 fractures for the three realizations R1, R2 and R3, which are indicated with red numbers. Notice that the number of fragments is smaller than the number of necks. The arrested necks, which are pointed with black arrows, seem to be unloaded by the release waves emanating from neighboring fractures, leading to long fracture-free segments, as suggested by Mott (1947), Kipp and Grady (1985) and Zhang and Ravi-Chandar (2006). In addition, the differences in the rate of development of the necks shown in Fig. 23 also seem to contribute to the heterogeneous spatial distribution of fractures. Fig. 25 shows histograms with the number of necks N_{neck} and the number of fragments N_{frag} versus the normalized Lagrangian neck spacing $\hat{L}_{neck}$ and the normalized Lagrangian fragment

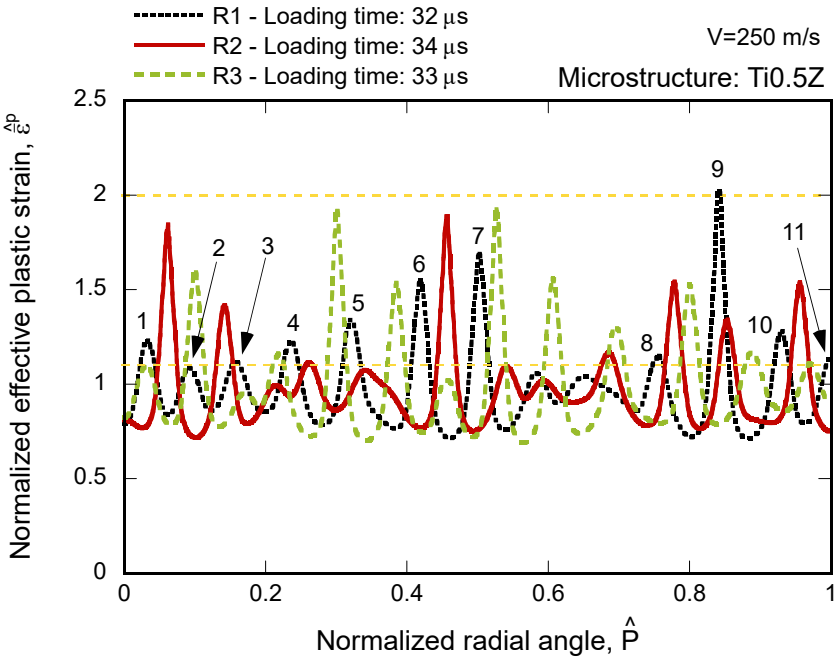

Figure 23: Normalized effective plastic strain $\hat{\varepsilon}^p$ versus normalized outer perimeter of the ring $\hat{P}$ for microstructure Ti0.5Z. Results are shown for 3 realizations of void size and position distribution: R1, R2 and R3. Loading velocity $V_r = 250$ m/s. The loading time is taken when the necking condition is met. Note that the necks corresponding to the realization R1 are numbered. The horizontal yellow dashed lines correspond to $\hat{\varepsilon}^p = 1.1$ and $\hat{\varepsilon}^p = 2$. For interpretation of the references to color in this figure, the reader is referred to the web version of this article.

size $\hat{L}_{frag} = \dfrac{L_{frag}}{h}$, respectively. The Lagrangian fragment size L_{frag} is defined as the distance between two consecutive fractures referred to the undeformed configuration. Taking together the results obtained for the three realizations, the normalized Lagrangian neck spacing varies from 2.87 to 12.04, and the average value of $\hat{L}_{neck}$ is 4.71, see Fig. 25(a). Note that 68% of the neck spacings lie within the interval $3.5 \leq \hat{L}_{neck} \leq 5.5$. On the other hand, the scatter in the fragments size is significantly greater, see Fig. 25(b), with $\hat{L}_{frag}$ varying from 8.35 to 18.71, being the average normalized fragment size 12.59. Notice that there are only two intervals, $9 \leq \hat{L}_{frag} \leq 10$ and $12 \leq \hat{L}_{frag} \leq 13$, for which we obtained more than one fragment, which illustrates the heterogeneous spatial distribution of fractures for this microstructure and loading velocity.

The influence of the porosity distribution on the necking and fragmentation is further illustrated in Fig. 26, which shows the evolution of the number of necks N_{neck} and fragments N_{frag} with the initial void volume fraction VF (%) and the maximum void diameter d_{max}. The loading velocity is $V_r = 250$ m/s. Results are included for all the microstructures investigated in this work. Similarly to the results obtained in Section 4 for the elastic perfectly-plastic material, see Fig. 19, the number of necks decreases with both initial void volume fraction and maximum void diameter. Namely, we have used a logarithmic function to fit the evolution of N_{neck} with the void volume fraction, which predicts that the number of necks drops $\approx 20\%$ within the range of values of VF (%) investigated.

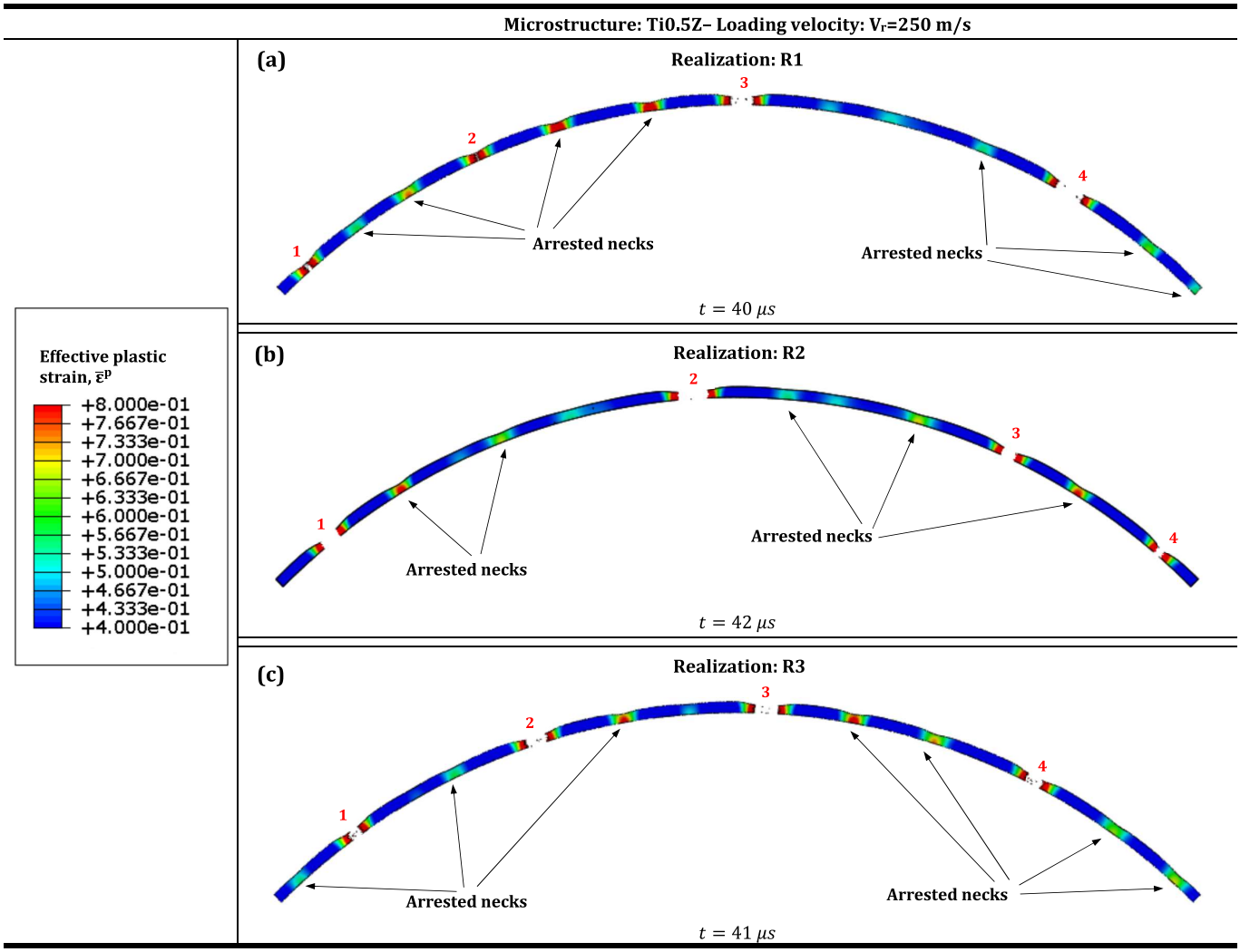

Figure 24: Contours of effective plastic strain $\bar{\varepsilon}^p$ for microstructure Ti0.5Z. Loading velocity $V_r = 250$ m/s. Cut view of the ring corresponding to the plane $Z = 0$. (a) Realization R1. Loading time $t = 40$ μs. (b) Realization R2. Loading time $t = 42$ μs. (c) Realization R3. Loading time $t = 41$ μs. For interpretation of the references to color in this figure, the reader is referred to the web version of this article.

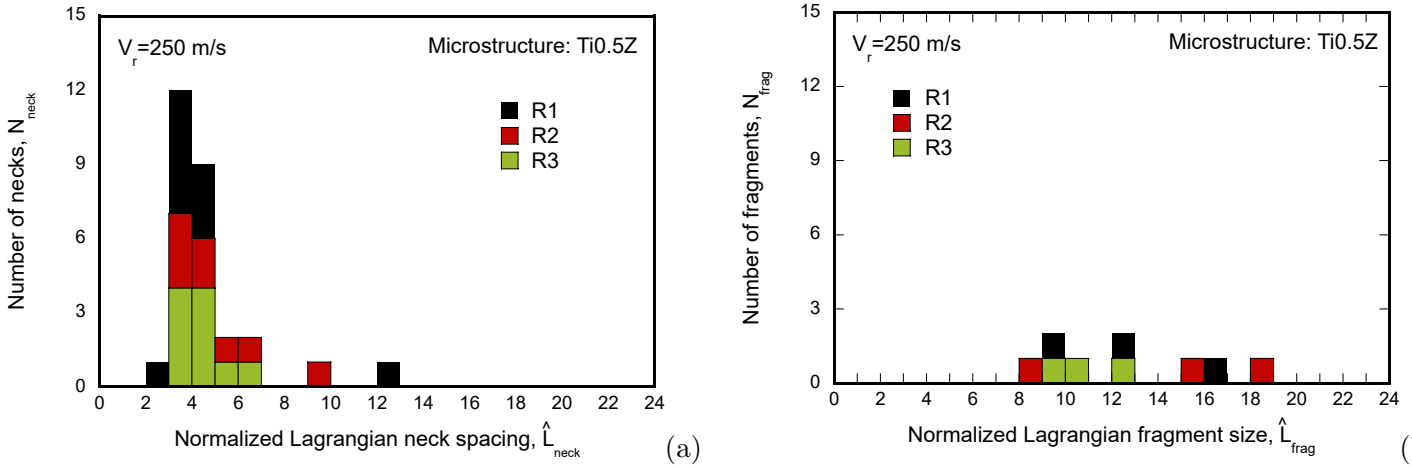

Figure 25: Histograms showing (a) the number of necks N_{neck} as a function of the normalized Lagrangian neck spacing $\hat{L}_{neck}$ and (b) the number of fragments N_{frag} as a function of the normalized Lagrangian fragment size $\hat{L}_{frag}$. The calculations correspond to the microstructure Ti0.5Z. Results are shown for 3 realizations of void size and position distribution: R1, R2 and R3. Loading velocity $V_r = 250$ m/s. Comparison between results obtained with three different loading velocities V_r: 50 m/s, 250 m/s and 500 m/s.

On the other hand, the decrease of the number of necks with the maximum void diameter d_{max} has been fitted with a linear function, based on which N_{neck} decreases from ≈ 10 to ≈ 6 within the range $25.90\ \mu s \leqslant d_{max} \leqslant 110.53\ \mu s$. In contrast, the number of fragments N_{frag} shows a slight increase with the initial void volume fraction and the maximum void diameter. It seems that, if the porosity is large and the material contains big voids, the proportion of necks that develop into fractures increases. Specifically, the logarithmic function used to fit the evolution of N_{frag} with VF (%) predicts that the number of fragments increases $\approx 25\%$ within the range of void volume fractions investigated. Moreover, the evolution of the number of fragments with the maximum void diameter has been fitted with a linear function, so that the predicted increase of N_{frag} with d_{max} is $\approx 20\%$. Nevertheless, we are aware that these trends should be further substantiated and evaluated in future works with additional finite element calculations.

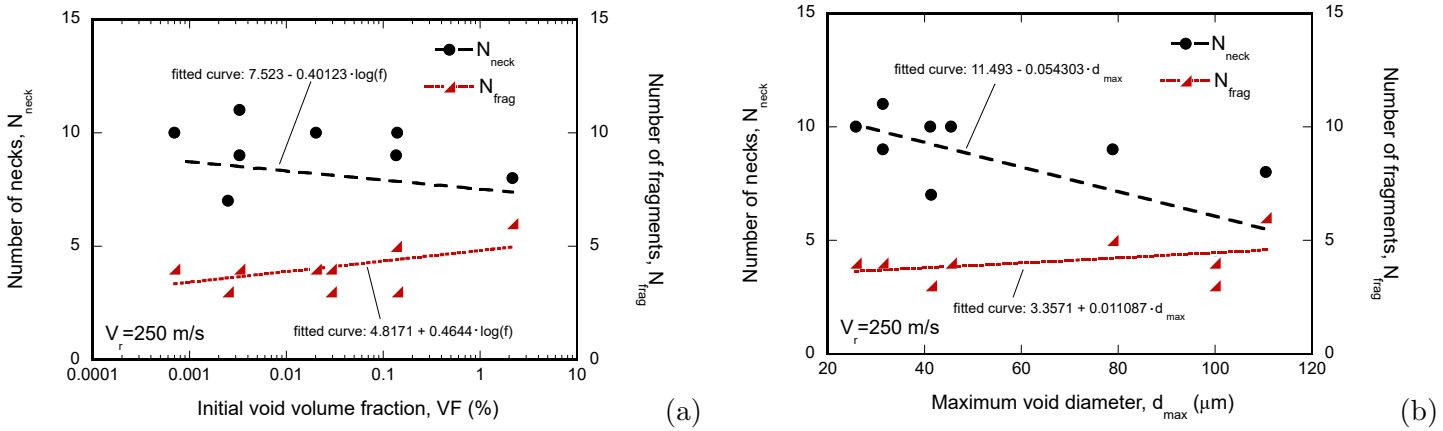

Figure 26: Number of necks N_{neck} and number of fragments N_{frag} versus: (a) initial void volume fraction VF (%) and (b) maximum void diameter d_{max}. Results are included for all the microstructures investigated in this work. The loading velocity is $V_r = 250$ m/s.

The evolution of the necking time t_{neck} and the fracture time t_{frac} with the initial void volume fraction VF (%) and the maximum void diameter d_{max} is shown in Fig. 27. The fracture time is taken as the loading time when the fracture condition $\bar{\varepsilon}_f^p = 1$ is first met (in any element of the mesh of the ring). Both necking time and fracture time decrease with the initial void volume fraction and the maximum void diameter, with t_{frac} being slightly greater than t_{neck} for the whole range of values of VF (%) and d_{max} investigated. As in the case of the elastic perfectly-plastic material, see Fig. 19, the evolution of the necking time with the initial void volume fraction and the maximum void diameter has been fitted with logarithmic and linear functions, respectively. Notice that the same functions, with different coefficients, have been used to fit the evolution of the fracture time with VF (%) and d_{max}.

The potential effect of strain hardening, strain rate hardening and thermal softening on the scatter in the

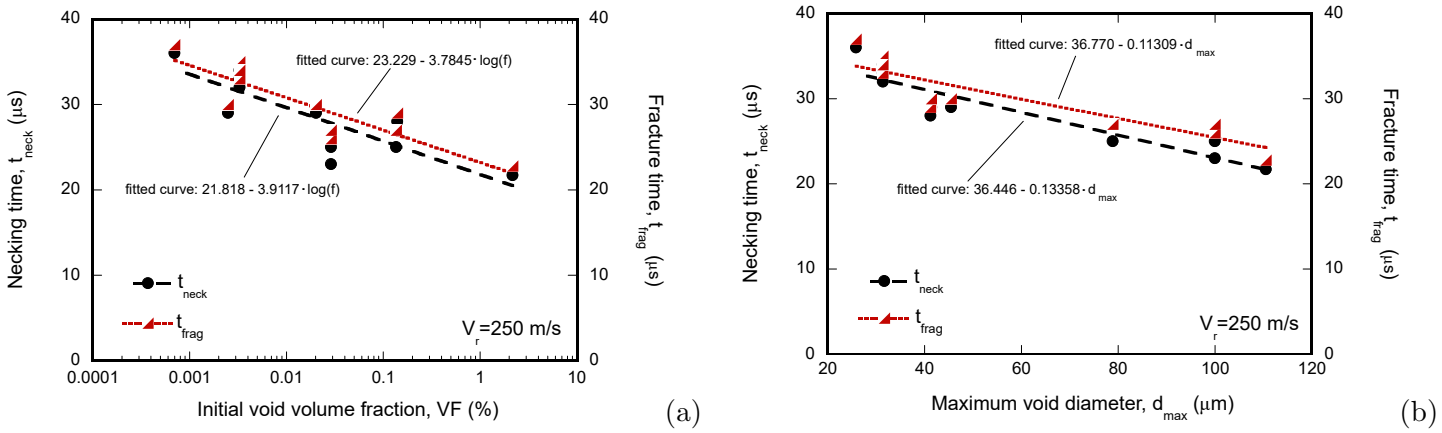

Figure 27: Necking time t_{neck} and fracture time t_{frag} versus: (a) initial void volume fraction VF (%) and (b) maximum void diameter d_{max}. Results are included for all the microstructures investigated in this work. The loading velocity is $V_r = 250$ m/s.

number of necks and fragments, and in the necking and fracture time, still needs further investigation. This is left for a future work.

5.2. The role of expansion velocity

Fig. 28 shows the normalized effective plastic strain $\hat{\bar{\varepsilon}}^p$ versus the normalized radial angle $\hat{P}$ for the microstructure INC1Z and realization R1. The INC1Z shows relatively large values for the void volume fraction and the maximum pore size, so that the microstructure has a marked effect on the necking and fragmentation patterns (especially for lower velocities, as discussed below). Calculations are shown for two different loading velocities $V_r = 175$ m/s and 325 m/s. The results obtained with the viscoplastic material with yield stress defined by equation (3) are compared with the calculations performed with the elastic perfectly-plastic material used in Section 4. The $\hat{\bar{\varepsilon}}^p - \hat{P}$ curves correspond to the loading time when the necking condition is met, being the necking time greater for the viscoplastic material, for both loading velocities, 175 m/s and 325 m/s, consistently with the results obtained for the microstructure Ti0.5Z (see Fig. 23 and the discussion therein). On the other hand, while the number of necks for 175 m/s is the same for both material models, in the case of 325 m/s the number of necks is less for the viscoplastic material, 9 versus 13, showing that the influence of the constitutive model in the number of necks depends on the loading velocity. Notice also that for $V_r = 175$ m/s the location of the necks is the same for both material models, reinforcing the idea that for the lower strain rates investigated in this paper the necking pattern is largely controlled by the porosity distribution. In contrast, for $V_r = 325$ m/s the spatial distribution of necks is markedly different for both material models, suggesting that at higher strain rates both mechanical behavior of the material and inertia play an important role in the distribution of neck spacings (porosity defects are not the sole factor controlling the necks location).

The influence of loading velocity in the distribution of neck spacings and fragment sizes for the microstructure INC1Z and the realization R1 is further illustrated in Fig. 29 which shows histograms with the number of necks

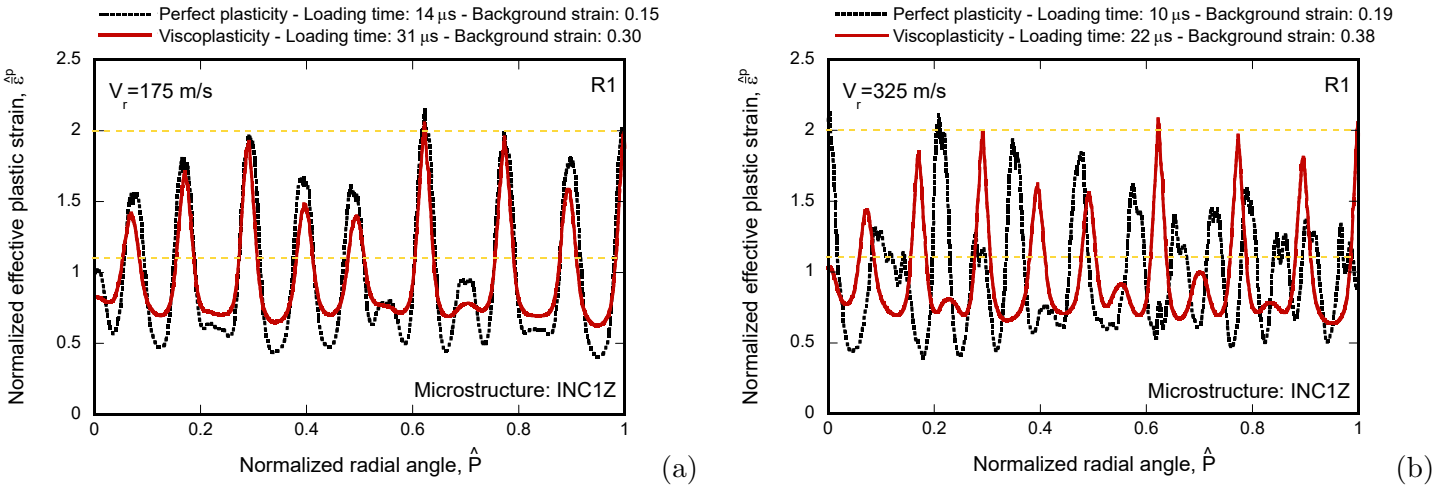

Figure 28: Normalized effective plastic strain $\hat{\varepsilon}^p$ versus normalized outer perimeter of the ring $\hat{P}$. Comparison between the elastic perfectly-plastic material used in Section 4, and the material with yield stress defined by equation (3). Finite element results obtained with the microstructure INC1Z and realization R1. Results corresponding to two different loading velocities V_r: (a) 175 m/s and (b) 325 m/s. The loading time is taken when the necking condition is met. The horizontal yellow dashed lines correspond to $\hat{\varepsilon}^p = 1.1$ and $\hat{\varepsilon}^p = 2$. For interpretation of the references to color in this figure, the reader is referred to the web version of this article.

N_{neck} and fragments N_{frag} versus the normalized Lagrangian neck spacing $\hat{L}_{neck}$ and the normalized Lagrangian fragment size $\hat{L}_{frag}$, respectively. The results correspond to three different velocities $V_r = 50$ m/s, 250 m/s and 500 m/s. The scatter in the size of the necks and fragments decreases with the loading velocity. Namely, for 50 m/s, the neck spacing varies within the range $5.72 < \hat{L}_{neck} < 15.48$, with an average value of 9.78. The scatter in the spatial distribution of necks is apparent in the contour plots shown in Fig. 30, where the necks nucleated in the ring are numbered. Note that only two of these five necks eventually grow until fracture, leading to the formation of long fragments. On the other hand, for 500 m/s, the necks spacing varies within a narrower range, namely $3.01 < \hat{L}_{neck} < 5.75$, with an average value of 4.27. The range of variation of the fragments size is relatively similar, $4.82 < \hat{L}_{frag} < 7.08$, because most of the necks incepted develop into fractures (8 fractures out of the 12 necks). Note that the ratio necks-to-fragments for 500 m/s (67%) is significantly greater than for 50 m/s (40%), illustrating that the spatial distribution of fractures is more uniform as the velocity increases. These results suggest that the stabilizing effect of inertia regularizes the necking pattern and enables the activation of additional fracture sites.

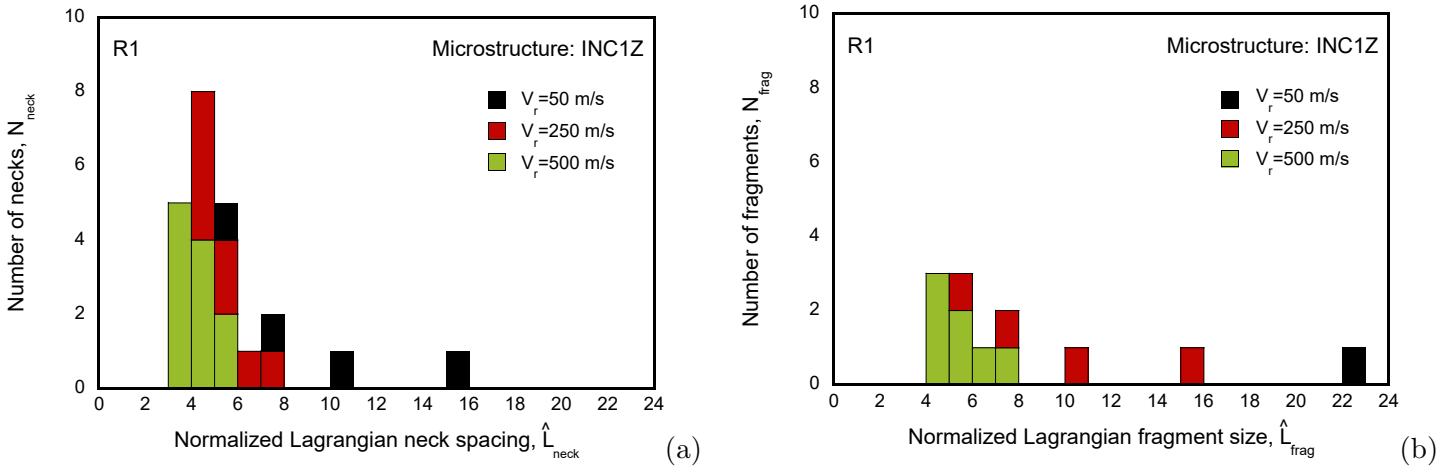

Figure 29: Histograms showing (a) the number of necks N_{neck} as a function of the normalized Lagrangian neck spacing $\hat{L}_{neck}$ and (b) the number of fragments N_{frag} as a function of the normalized Lagrangian fragment size $\hat{L}_{frag}$. The calculations correspond to the microstructure INC1Z and the realization R1. Comparison between results obtained with three different loading velocities V_r: 50 m/s, 250 m/s and 500 m/s.

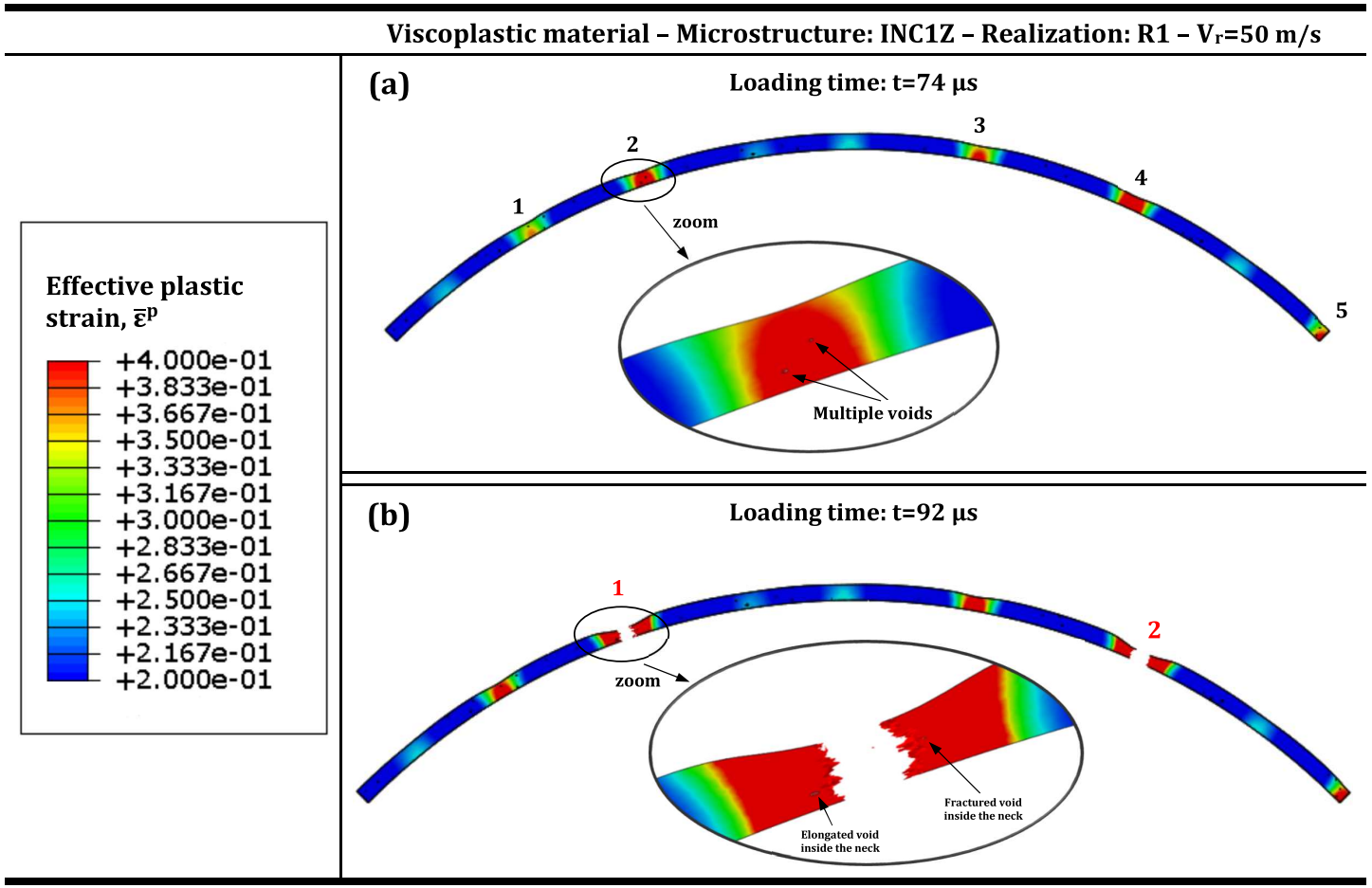

Figure 30: Contours of effective plastic strain $\bar{\varepsilon}^p$ for microstructure INC1Z. Realization R1. Cut view of the ring corresponding to the plane $Z = 0$. Loading velocity $V_r = 50$ m/s. (a) Loading time $t = 74$ μs. (b) Loading time $t = 92$ μs.

Fig. 31 shows the evolution of the average normalized Lagrangian neck spacing $\hat{L}^{avg}_{neck}$ and the average normalized Lagrangian fragment size $\hat{L}^{avg}_{frag}$ versus the inertia parameter $\hat{H}^{-1}$ for finite element results obtained with the microstructure INC1Z and realization R1. Recall from Section 4 that the inertia parameter does not include explicitly the potential effect of strain hardening, strain rate hardening and thermal softening on the necking behavior of the materials, since it only accounts for a reference stress level. Recall also from Section 4.2 that $\hat{L}^{avg}_{neck} = \dfrac{\pi R_{ext}}{2hN_{neck}}$, and similarly $\hat{L}^{avg}_{frag} = \dfrac{\pi R_{ext}}{2hN_{frag}}$. A comparison is performed with the ring expansion experiments carried out by Grady and Benson (1983) with Aluminium $1100-\mathrm{O}$ and OFHC copper specimens. Note that the reference stress level used to compute the value of the inertia parameter in the experiments of Grady and Benson (1983) is obtained from the static characterization tests reported therein. There is reasonable qualitative and quantitative agreement between finite elements and experimental data, notably for the results for with Aluminium $1100-\mathrm{O}$, which practically overlap with the numerical calculations. This agreement may suggest that the neck spacing and fragment size is more sensitive to inertia than to porosity on the one hand and to constitutive behavior (strain and strain rate sensitivity) on the other hand. Nevertheless, this conclusion should be substantiated in future works with additional experimental and numerical results. The finite element results for the average normalized Lagrangian neck spacing and the average normalized Lagrangian fragment size are fitted with the functions $\hat{L}^{avg}_{neck} = 1.7898\left(\frac{1}{\hat{H}}\right)^{-0.3}$ and $\hat{L}^{avg}_{frag} = 1.5946\left(\frac{1}{\hat{H}}\right)^{-0.51}$, respectively, illustrating the nonlinear decrease of both $\hat{L}^{avg}_{neck}$ and $\hat{L}^{avg}_{frag}$ with the increase of inertia (consistent with the trends obtained in other experiments available in the literature, see Zhang and Ravi-Chandar (2006)). Notice that the gap between $\hat{L}^{avg}_{neck}$ and $\hat{L}^{avg}_{frag}$ predicted by the finite elements gradually decreases as $\hat{H}^{-1}$ increases, in agreement with the calculations reported by Rodríguez-Martínez et al. (2013a) and Vaz-Romero et al. (2019).

6. Summary and conclusions

In this paper we have developed a novel methodology to identify the effect of porous microstructure on dynamic localization and fragmentation of ductile metallic materials. Firstly, we have performed X-ray tomography of 12 additively manufactured cylindrical specimens with diameter and height of 6 mm made of 4 different materials –aluminium alloy $\mathrm{AlSi_{10}Mg}$, stainless steel 316L, titanium alloy $\mathrm{Ti_6Al_4V}$ and Inconel 718L– that were printed of parallel and perpendicular to the longitudinal axis of the samples. The tomograms have shown that the initial void volume fraction of the specimens varies between $\approx 0.0007\%$ and $\approx 2\%$, with the pores being nearly spherical for most of the samples, with diameter ranging from ≈ 6 μm to ≈ 110 μm. The pore size distributions recorded in the 12 tomograms have been fitted to a Log-normal statistical function, which has been used in conjunction with a Force Biased Algorithm that models the experimentally observed random spatial distribution of the voids, to generate

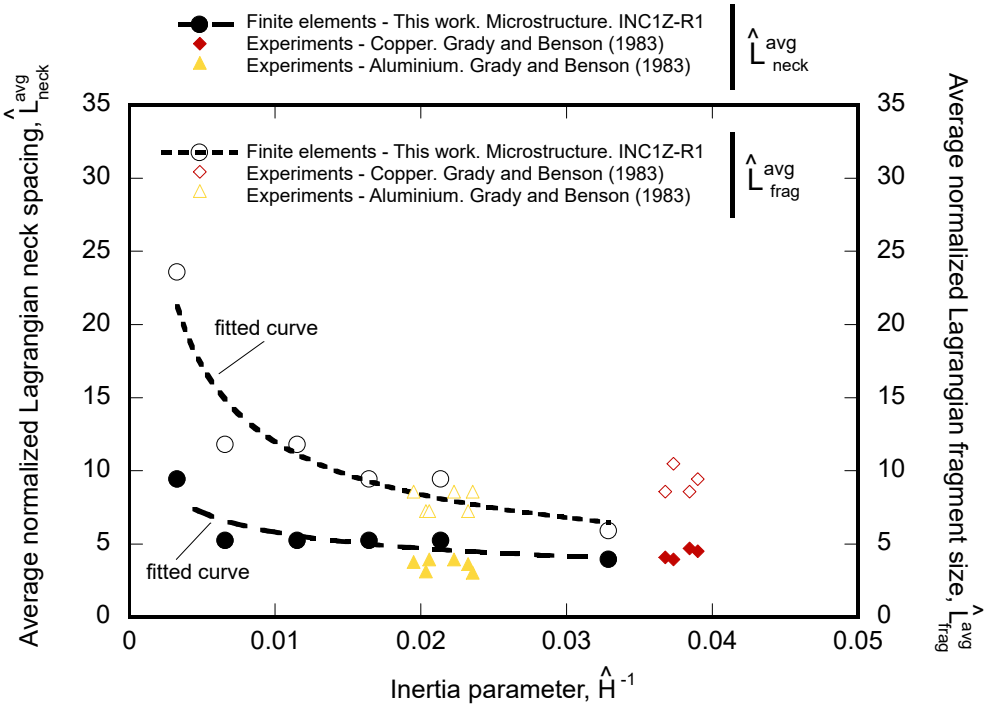

Figure 31: Average normalized Lagrangian neck spacing $\hat{L}^{avg}_{neck}$ and average normalized Lagrangian fragment size $\hat{L}^{avg}_{frag}$ versus inertia parameter $\hat{H}^{-1}$. Finite element results obtained in this work for the microstructure INC1Z with realization R1. Comparison with the ring expansion experiments carried out by Grady and Benson (1983) with Aluminium $1100-O$ and OFHC copper specimens. The finite element results obtained in this work for the average normalized Lagrangian neck spacing and the average normalized Lagrangian fragment size are fitted with the curves $\hat{L}^{avg}_{neck} = 1.7898\left(\frac{1}{\hat{H}}\right)^{-0.3}$ and $\hat{L}^{avg}_{frag} = 1.5946\left(\frac{1}{\hat{H}}\right)^{-0.51}$, respectively.

ring expansion finite element models in ABAQUS/Explicit (2016) which include actual porous microstructures representative of the materials tested. For each of the 12 porous microstructures analyzed, we have generated three realizations of void size and position distribution fulfilling the same Log-normal function parameters in order to take into account the potential scatter in the finite element results coming from the randomness in spatial void dispersion. The finite element calculations have been carried out for expansion velocities ranging from 50 m/s to 500 m/s, and the material behavior has been modeled using isotropic linear elasticity and von Mises plasticity.

The calculations carried out to identify the role of porous microstructure on dynamic localization have been performed considering ideal plasticity, so that the formation of multiple necks is solely controlled by stress multiaxiality, inertia and porosity, which facilitates the interpretation of results. Indeed, we have shown that both porous microstructure and inertia play a main role in the resulting necking patterns, so that while the microstructure imposes the nucleation of necks at specific locations (weak points) of the specimen for all the velocities investigated, inertia delays localization and favors the formation of additional necks at higher loading rates. In addition, we have established individualized correlations between the main features of the porous microstructure and the necking pattern. Specifically, the finite element calculations have shown that both number of necks and necking time decrease linearly with the logarithm of the void volume fraction and with the maximum diameter of the voids,

this decrease being more pronounced for the necking time $\approx 120\%$ than for the number of necks $\approx 20\%$. On the other hand, while the increase of the average size of the voids also leads to a decrease of $\approx 20\%$ in the number of necks, it does not show any connection with the necking time for the porous microstructures investigated in this work.

The calculations carried out to investigate the influence of porous microstructure on dynamic fragmentation have been performed considering that the yield stress evolves with the effective plastic strain, the effective plastic strain rate and the temperature. In addition, we have assumed adiabatic conditions of deformation, and a failure criterion based on the element deletion technique available in ABAQUS/Explicit (2016) so that material fails when a critical value of the accumulated plastic strain is reached. Like the necking time, the fracture time decreases linearly with the logarithm of the void volume fraction and with the maximum diameter of the voids. In contrast, the number of fragments, unlike the number of necks, slightly increases with the level of porosity in the specimen and the maximum size of the pores. On the one hand, the resemblance with the results obtained for the elastic perfectly-plastic material suggest that the relationships found out in this paper between porosity, nucleation of necks and formation of fragments are valid for different material behaviors. On the other hand, we are aware that additional finite element simulations shall be performed in future works to further substantiate the conclusions obtained in this work. The finite element calculations have also shown that as the loading rate increases the number of fragments and the proportion of necks that develop into fractures increases, reducing the scatter in the distribution of fragment sizes. These results suggest that the stabilizing effect of inertia regularizes the necking pattern and enables the activation of additional fracture sites. In addition, the finite element results have been compared with the ring expansion experiments performed by Grady and Benson (1983) with aluminium and copper specimens, and reasonable qualitative and quantitative agreement has been found for the average neck spacing and the average fragment size.

In summary, the methodology developed in this paper can be used to obtain new insights into the performance of additively manufactured metals in energy absorption applications where protective structures are subjected to impact and shock loading (Kristoffersen et al., 2020). A future work is to perform additional simulations with controlled and systematic variation of the void volume fraction and the maximum void size (e.g. fixed pores size and different void volume fractions, fixed void volume fraction and different voids size, etc.) to obtain additional insights into the microstructural features that control the localization and fragmentation processes. Moreover, it has to be highlighted that the conclusions derived in this paper are substantiated on the basis of rather simple descriptions of the constitutive behavior of the material. In this regard, a natural continuation of this research is to consider constitutive models which account for the specific features which characterize the mechanical behavior of

metallic printed materials, including plastic anisotropy and tension/compression asymmetry (Ghorbanpour et al., 2020; Ferreri et al., 2019). On the other hand, since the size of the pores may be of the order of magnitude of the material grains (Liu et al., 2019), using crystal plasticity to describe the mechanical behavior of the matrix material would allow to include additional microstructural features into the finite element models developed in this paper, see Dequiedt and Denoual (2021). In addition, the microstructurally-informed finite element models devised in this work can be employed to validate dynamic porous plasticity theories, like the microinertia-based approach developed by Molinari and co-workers (Molinari and Mercier, 2001; Czarnota et al., 2008), which are generally used to determine flow and fracture of porous materials at high strain rates (Czarnota et al., 2017, 2020).

Acknowledgements

The research leading to these results has received funding from the European Research Council (ERC) under the European Union's Horizon 2020 research and innovation programme. Project PURPOSE, grant agreement 758056.

J.A.R.-M expresses sincere gratitude to Professor Alain Molinari (University of Lorraine, France) for multitude discussions on dynamic localization and fragmentation of metallic materials.

References

ABAQUS/Explicit, 2016. Abaqus Explicit v6.16 User's Manual. ABAQUS Inc., Richmond, USA.

Aboulkhair, N.T., Everitt, N.M., Ashcroft, I., Tuck, C., 2014. Reducing porosity in alsi10mg parts processed by selective laser melting. Additive Manufacturing 1-4, 77 – 86. Inaugural Issue.

Bargieł, M., Mościński, J., 1991. C-language program for the irregular close packing of hard spheres. Computer Physics Communications 64, 183–192.

Becker, R., Callaghan, K., 2018. Evaluation of gurson yield function dependencies through large-scale void growth simulations. International Journal of Fracture 209, 235–240.

Becker, R., Callaghan, K., 2020. Void growth dependence on loading path and mean stress from large-scale numerical simulations. International Journal of Plasticity 134, 102780.

Bolte, S., Cordeliéres, F.P., 2006. A guided tour into subcellular colocalization analysis in light microscopy. Journal of Microscopy 224, 213–232.

Bridgman, P.W., 1952. Studies in large plastic flow and fracture, with special emphasis on the effects of hydrostatic pressure, vol.1. McGraw-Hill Book Company, Inc., New York.

Chung, K., Wagoner, R.H., 1988. Effects of work-hardening and rate sensitivity on the sheet tensile test. Metallurgical and Material Transactions A 19, 293–300.

Cliche, N., Ravi-Chandar, K., 2018. Dynamic strain localization in magnesium alloy AZ31B-O. Mechanics of Materials 116, 189 – 201. IUTAM Symposium on Dynamic Instabilities in Solids.

Czarnota, C., Jacques, N., Mercier, S., Molinari, A., 2008. Modelling of dynamic ductile fracture and application to the simulation of plate impact tests on tantalum. Journal of the Mechanics and Physics of Solids 56, 1624 – 1650.

Czarnota, C., Molinari, A., Mercier, S., 2017. The structure of steady shock waves in porous metals. Journal of the Mechanics and Physics of Solids 107, 204–228.

Czarnota, C., Molinari, A., Mercier, S., 2020. Steady shock waves in porous metals: Viscosity and micro-inertia effects. International Journal of Plasticity 135, 102816.

Dequiedt, J.L., 2015. Statistics of dynamic of dynamic fragmentation for a necking instability. International Journal of Solids and Structures 32-44, 107–120.

Dequiedt, J.L., Denoual, C., 2021. Localization of plastic deformation in stretching sheets with a crystal plasticity approach: Competition between weakest link and instable mode controlled process. International Journal of Solids and Structures 210–211, 183–202.

Ferreri, N.C., Ghorbanpour, S., Bhowmik, S., Lussier, R., Bicknell, J., Patterson, B.M., Knezevic, M., 2019. Effects of build orientation and heat treatment on the evolution of microstructure and mechanical properties of alloy mar-m-509 fabricated via laser powder bed fusion. International Journal of Plasticity 121, 116 – 133.

Fressengeas, C., Molinari, A., 1994. Fragmentation of rapidly stretching sheets. European Journal of Mechanics A/Solids 13, 251–268.

Ghorbanpour, S., Alam, M.E., Ferreri, N.C., Kumar, A., McWilliams, B.A., Vogel, S.C., Bicknell, J., Beyerlein, I.J., Knezevic, M., 2020. Experimental characterization and crystal plasticity modeling of anisotropy, tension-compression asymmetry, and texture evolution of additively manufactured Inconel 718 at room and elevated temperatures. International Journal of Plasticity 125, 63 – 79.

Grady, D., 2002. Fragmentation of expanding cylinders and the statistical theory of N. F. Mott. AIP Conference Proceedings 620, 799–802.

Grady, D.E., 1981. Fragmentation of solids under impulsive stress loading. Journal of Geophysical Research: Solid Earth 86, 1047–1054.

Grady, D.E., Benson, D.A., 1983. Fragmentation of metal rings by electromagnetic loading. Experimental Mechanics 12, 393–400.

Grady, D.E., Olsen, M.L., 2003. A statistics and energy based theory of dynamic fragmentation. International Journal of Impact Engineering 29, 293–306.

Guduru, P.R., Freund, L.B., 2002. The dynamics of multiple neck formation and fragmentation in high rate extension of ductile materials. International Journal of Solids and Structures 39, 5615–5632.

Gurson, A., 1977. Continuum theory of ductile rupture by void nucleation and growth. Part I: Yield criteria and flow rules for porous ductile media. ASME Journal of Engineering Materials and Technology 99, 2–15.

Habib, S.A., Lloyd, J.T., Meredith, C.S., Khan, A.S., Schoenfeld, S.E., 2019. Fracture of an anisotropic rare-earth-containing magnesium alloy (ZEK100) at different stress states and strain rates: Experiments and modeling. International Journal of Plasticity 122, 285 – 318.

Hill, R., 1952. On discontinous plastic states, with special reference to localized necking in thin sheets. Journal of the Mechanics and Physics of Solids 1, 19–30.

Hiroe, T., Fujiwara, K., Hata, H., Takahashi, H., 2008. Deformation and fragmentation behaviour of exploded metal cylinders and the effects of wall materials, configuration, explosive energy and initiated locations. International Journal of Impact Engineering 35, 1578–1586.

Hutchinson, J.W., Neale, K., 1977. Influence of strain rate sensitivity on necking under uniaxial tension. Acta Metallurgica 25, 839–846.

Kasperovich, G., Haubrich, J., Gussone, J., Requena, G., 2016. Correlation between porosity and processing parameters in tial6v4 produced by selective laser melting. Materials & Design 105, 160 – 170.

Khan, A.S., Liu, H., 2012. Strain rate and temperature dependent fracture criteria for isotropic and anisotropic metals. International Journal of Plasticity 37, 1 – 15.

Kipp, M.E., Grady, D.E., 1985. Dynamic fracture growth and interaction in one dimension. Journal of the Mechanics and Physics of Solids 33, 399–415.

Koutiri, I., Pessard, E., Peyre, P., Amlou, O., De Terris, T., 2018. Influence of SLM process parameters on the surface finish, porosity rate and fatigue behavior of as-built inconel 625 parts. Journal of Materials Processing Technology 255, 536 – 546.

Kristoffersen, M., Costas, M., Koenis, T., Brøtan, V., Paulsen, C.O., Borvik, T., 2020. On the ballistic perforation resistance of additive manufactured alsi10mg aluminium plates. International Journal of Impact Engineering 137, 103476.

Li, Z., Li, Z., Tan, Z., Xiong, D.B., Guo, Q., 2020. Stress relaxation and the cellular structure-dependence of plastic deformation in additively manufactured AlSi10Mg alloys. International Journal of Plasticity 127, 102640.

Li, Z., Voisin, T., McKeown, J.T., Ye, J., Braun, T., Kamath, C., King, W.E., Wang, Y.M., 2019. Tensile properties, strain rate sensitivity, and activation volume of additively manufactured 316L stainless steels. International Journal of Plasticity 120, 395 – 410.

Liu, M., Guo, Z., Fan, C., Tang, T., Wang, X., Hu, H., 2016. Modeling spontaneous shear bands evolution in thick-walled cylinders subjected to external high-strain-rate loading. International Journal of Solids and Structures 97-98, 336 – 354.

Liu, M., Li, Y., Hu, H., Hu, X., 2013. A numerical model for adiabatic shear bands with application to a thick-walled cylinder in 304 stainless steel. Modelling and Simulation in Materials Science and Engineering 22, 015005.

Liu, X., Zhao, C., Zhou, X., Shen, Z., Liu, W., 2019. Microstructure of selective laser melted alsi10mg alloy. Materials & Design 168, 107677.

Marvi-Mashhadi, M., Lopes, C., LLorca, J., 2020. High fidelity simulation of the mechanical behavior of closed-cell polyurethane foams. Journal of the Mechanics and Physics of Solids 135, 103814.

Marvi-Mashhadi, M., Rodríguez-Martínez, J.A., 2020. Multiple necking patterns in elasto-plastic rings subjected to rapid radial expansion: The effect of random distributions of geometric imperfections. International Journal of Impact Engineering 144, 103661.

Mercier, S., Granier, N., Molinari, A., Llorca, F., Buy, F., 2010. Multiple necking during the dynamic expansion of hemispherical metallic shells, from experiments to modelling. Journal of the Mechanics and Physics of Solids 58, 955–982.

Mercier, S., Molinari, A., 2004. Analysis of multiple necking in rings under rapid radial expansion. International Journal of Impact Engineering 30, 403–419.

Molinari, A., Mercier, S., 2001. Micromechanical modelling of porous materials under dynamic loading. Journal of the Mechanics and Physics of Solids 49, 1497 – 1516.

Mott, N.F., 1947. Fragmentation of shell cases. Proceedings of the Royal Society of London. Series A. Mathematical and Physical Sciences 189, 300–308.

Moussaoui, K., Rubio, W., Mousseigne, M., Sultan, T., Rezai, F., 2018. Effects of selective laser melting additive manufacturing parameters of inconel 718 on porosity, microstructure and mechanical properties. Materials Science and Engineering: A 735, 182 – 190.

Needleman, A., 1991. The effect of material inertia on neck development. In: Yang, W.H. (Ed.), Topics in Plasticity. AM Press, Ann Arbor, MI , 151–160.

N'souglo, K.E., Rodríguez-Martínez, J.A., Cazacu, O., 2020. The effect of tension-compression asymmetry on the formation of dynamic necking instabilities under plane strain stretching. International Journal of Plasticity 128, 102656.

N'souglo, K.E., Srivastava, A., Osovski, S., Rodríguez-Martínez, J.A., 2018. Random distributions of initial porosity trigger regular necking patterns at high strain rates. Proceedings of the Royal Society A: Mathematical, Physical and Engineering Sciences 474, 20170575.

Pandya, K.S., Roth, C.C., Mohr, D., 2020. Strain rate and temperature dependent fracture of aluminum alloy 7075: Experiments and neural network modeling. International Journal of Plasticity 135, 102788.

Rodríguez-Martínez, J.A., Molinari, A., Zaera, R., Vadillo, G., Fernández-Sáez, J., 2017. The critical neck spacing in ductile plates subjected to dynamic biaxial loading: on the interplay between loading path and inertia effects. International Journal of Solids and Structures 108, 74–84.

Rodríguez-Martínez, J.A., Vadillo, G., Fernández-Sáez, J., Molinari, A., 2013a. Identification of the critical wavelength responsible for the fragmentation of ductile rings expanding at very high strain rates. Journal of the Mechanics and Physics of Solids 61, 1357–1376.

Rodríguez-Martínez, J.A., Vadillo, G., Zaera, R., Fernández-Sáez, J., 2013b. On the complete extinction of selected imperfection wavelengths in dynamically expanded ductile rings. Mechanics of Materials 60, 107–120.

Rusinek, A., Zaera, R., 2007. Finite element simulation of steel ring fragmentation under radial expansion. International Journal of Impact Engineering 34, 799–822.

Schneider, C.A., Rasband, W.S., Eliceiri, K.W., 2012. Nih image to imagej: 25 years of image analysis. Nature methods 9, 671–675.

Stef, J., Poulon-Quintin, A., Redjaimia, A., Ghanbaja, J., Ferry, O., De Sousa, M., Gouné, M., 2018. Mechanism of porosity formation and influence on mechanical properties in selective laser melting of Ti-6Al-4V parts. Materials & Design 156, 480 – 493.

Sukal, J., Palousek, D., Koutny, I., 2018. The effect of recycling powder steel of porosity and surface roughness of SLM parts. MM Science Journal , 2643 – 2647.

Tancogne-Dejean, T., Roth, C.C., Woy, U., Mohr, D., 2016. Probabilistic fracture of Ti–6Al–4V made through additive layer manufacturing. International Journal of Plasticity 78, 145 – 172.

Tvergaard, V., 1981. Influence of voids on shear band instabilities under plane strain conditions. International Journal of Fracture 17, 389–407.

Tvergaard, V., 1982. On localization in ductile materials containing spherical voids. International Journal of Fracture 18, 237–252.

Vadillo, G., Rodríguez-Martínez, J.A., Fernández-Sáez, J., 2012. On the interplay between strain rate and strain rate sensitivity on flow localization in the dynamic expansion of ductile rings. International Journal of Solids and Structures 49, 481–491.

Vaz-Romero, A., Mercier, S., Rodríguez-Martínez, J.A., Molinari, A., 2019. A comparative study of the dynamic fragmentation of non-linear elastic and elasto-plastic rings: The roles of stored elastic energy and plastic dissipation. Mechanics of Materials 132, 134–148.

Vaz-Romero, A., Rodríguez-Martínez, J.A., Arias, A., 2015. The deterministic nature of the fracture location in the dynamic tensile testing of steel sheets. International Journal of Impact Engineering 86, 318 – 335.

Vaz-Romero, A., Rodríguez-Martínez, J.A., Mercier, S., Molinari, A., 2017. Multiple necking pattern in nonlinear elastic bars subjected to dynamic stretching: The role of defects and inertia. International Journal of Solids and Structures 125, 232 – 243.

Wesenberg, D., Sagartz, M., 1977. Dynamic fracture of 6061-T6 aluminium cylinders. Journal of Applied Mechanics 44, 643–646.

Xue, Z., Vaziri, A., Hutchinson, J.W., 2008. Material aspects of dynamic neck retardation. Journal of the Mechanics and Physics of Solids 56, 93–113.

Zhang, B., Li, Y., Bai, Q., 2017. Defect formation mechanisms in Selective Laser Melting: A review. Chinese Journal of Mechanical Engineering 30, 515 – 527.

Zhang, H., Ravi-Chandar, K., 2006. On the dynamics of necking and fragmentation - I. Real-time and post-mortem observations in Al 6061-O. International Journal of Fracture 142, 183–217.

Zhang, H., Ravi-Chandar, K., 2008. On the dynamics of necking and fragmentation - II. Effect of material properties geometrical constraints and absolute size. International Journal of Fracture 150, 3–36.

Zhang, H., Ravi-Chandar, K., 2010. On the dynamics of localization and fragmentation-IV. Expansion of Al 6061-O tubes. International Journal of Fracture 163, 41–65.

Zhou, F., Molinari, J.F., Ramesh, K.T., 2006. An elasto-visco-plastic analysis of ductile expanding ring. International Journal of Impact Engineering 33, 880–891.